Defect states in MAPbBr$_3$ by Photo-Induced Current Transient Spectroscopy

Supervisor:
Prof. Daniela Cavalcoli

Co-supervisor:
Dr. Giovanni Armaroli

Dr. Lorenzo Maserati

Submitted by:
Martina Foschi

Academic Year 2020/2021

*Uber Halbleiter sollte man nicht
arbeiten, das ist eine
Schweinerei, wer weis ob es
überhaupt Halbleiter gibt.*

One should not work on
semiconductors. They are a
mess. Who knows whether
semiconductors exist at all.
W. Pauli 1931

Abstract

In the past decade, perovskites have been under the spotlight as promising semiconductors with unique properties. Hybrid halide perovskites show excellent characteristic properties suitable for optoelectronic applications as tunable band gap, high absorption coefficient, large mobility and long carrier recombination lifetime. However, a complete understanding of environmental instability and the nature of defects in these materials is still lacking, hindering the development of perovskite-based technologies. In this work we studied $MAPbBr_3$ single crystals, fabricated with Inverse Temperature Crystallization (ITC) technique, with Photo-Induced Current Transient Spectroscopy (PICTS). PICTS is a transient photocurrent measurement rarely employed for studying perovskites materials, that allows for the defects characterization in high resistivity materials. We studied the samples under different conditions, such as negative and positive voltage biases, bias stress, different contact geometries and different illumination wavelengths, in order to study their effect on the material physical properties and to evaluate the trap activation energies and their behavior under different working conditions.

Contents

Introduction

In the past decade perovskites has been in the spotlight as promising semiconductors with unique properties. Perovskites are a class of compounds following the same simple crystal structure ABX_3 of calcium titanium oxide mineral ($CaTiO_3$), where A, B and X are different chemical elements. Among all the species, hybrid halide perovskites show excellent characteristic properties suitable for optoelectronic applications as tunable band gap, high absorption coefficient, large mobility and long carrier recombination lifetime. These materials comprise an halide X anion as bromine, chlorine or iodine and an organic A cation as methylammonium (MA) or formamidinium (FA), thus exploiting the characteristics of both organic and inorganic compounds. Thanks to their excellent properties perovskites are employed in several optoelectronic applications as solar cells, ionizing radiation detectors and LEDs.

Despite the advances in the study of perovskites devices two main issues remain to be solved: stability and defect control. The instability to moisture, oxygen and temperature, just to cite some, is one of the main barrier to commercialization of perovskite-based devices. On the other hand, as defects affect the charge transport properties, the understanding of their nature and energy scale is therefore crucial for the development and optimization of perovskites based devices. Having information on defects parameters is the key to design defect control strategies and to understand the impact that defects play on stability and transport properties. For this reason this work is focused on the study of defects states performing Photo-Induced Current Transient Spectroscopy (PICTS), a transient measurement technique, on $MAPbBr_3$ hybrid halide perovskite. As this technique has never being used to investigate perovskites compounds, we performed several measurements in different conditions to study not only the defects activation energies, but also the material response.

The first chapter of this work presents hybrid halide perovskites giving an outcome of their properties, stability issues and applications. Chapter 2 delineates the physical principles on which transient measurement techniques are based, focusing then on the mechanisms underlying the Photo-Induced Current Transient Spectroscopy. The fabrication method employed to produce $MAPbBr_3$ single crystal is described in the third chapter. Chapter 3 also describes the PICTS experimental set-up and the data processing methods used to analyse transient measurements data. Finally, in Chapter 4 the

main results are presented. We firstly tested the PICTS data processing methods on a known stable semiconductor. Then, we performed PICTS on MAPbBr$_3$ single crystals, varying measurement working conditions, contact geometry of the samples and probing wavelength.

Chapter 1

Hybrid perovskites: structure and properties

Perovskites are a class of compounds with a simple crystal structure expressed as ABX_3, where A, B and X are different chemical elements. This class of materials takes its name from the structure of calcium titanium oxide mineral ($CaTiO_3$), discovered in Ural mountains of Russia by Gustav Rose in 1839 and named after Russian mineralogist Lev Perovski.

In the past decade, hybrid halide perovskites have been in the spotlight as promising semiconductor for optoelectronic devices. Hybrid halide perovskites comprise both organic and inorganic properties, comprising an halide X anion and an organic A cation. Thanks to their unique physical properties as high absorption coefficient, long-range charge transport and tunable energy gap, they have emerged as most promising, efficient and low cost materials for photovoltaic applications, leading to a steep increase of solar cell power conversion efficiency. Since perovskites are regarded as a class of materials, it is easy to understand the extent of properties achievable by different types of these compounds. Among all, hybrid metal halide perovskites, i.e. where B is the metallic element, have gained huge attention thanks to their suitable energy band gap for photovoltaic applications. An example is methyl-ammonium lead iodide ($MAPbI_3$), the most popular material used as active layer in solar cells, with an energy gap of 1.55 eV. Another case of interest is methyl-ammonium lead bromide ($MAPbBr_3$), not suitable for photovoltaic application because of its too high energy band gap of 2.3 eV, but ideal for radiation detection because of large mobility, carrier life time and high atomic numbers of Pb and Br. Moreover, the higher band gap of $MAPbBr_3$ leads to lower thermal noise, hence lower dark current and therefore higher signal to noise ratio. In the following pages structural, optical and transport properties of perovskites will be presented, with particular attention on $MAPbBr_3$ perovskite.

1.1 Crystal structure of hybrid perovskite

In the cubic ABX_3 perovskites, an A-site cation is confined in a cage structure formed by B-site cations and X-site anions. B atom si sixfold coordinated with X atoms, creating a BX_6 octahedron that is interconnected via all corners to form a three-dimensional perovskite network (Figure 1.1). In particular, hybrid halide perovskites comprise a monovalent organic A-site cation ($CH_3NH_3^+$ or $HC(NH_2)_2^+$), divalent B-site group IV cations (Pb^{2+}, Sn^{2+} and Ge^{2+}) and X-site halide anions (Br^-, I^-, Cl^-), so that charge neutrality is expressed as $A^+B^{2+}(X^-)_3$. In methyl-ammonium lead bromide the Pb^{2+} cation acts as the anchor of the cubic perovskite unit cell, located at the body center $[\frac{1}{2}\frac{1}{2}\frac{1}{2}]$. The eight organic cations MA^+ are located at the corners of the cubic unit cell $[000]$, where each of them contributes to $\frac{1}{8}$ of the volume as each of the cations is connected to eight other unit cells. Lastly, twelve Bromide anion Br^- are located at $(\frac{1}{2}\frac{1}{2}0)$, $(\frac{1}{2}0\frac{1}{2})$ and $(0\frac{1}{2}\frac{1}{2})$, each contributing only $\frac{1}{4}$.
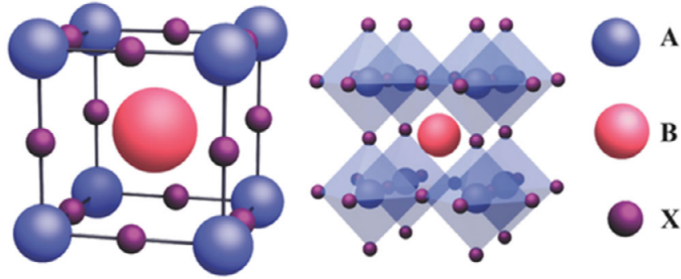

Figure 1.1: *Unit cell of cubic perovskite crystal following* ABX_3 *structure (left). Extended perovskite crystalline structure (right) [1].*

Depending on temperature, $MAPbBr_3$ hybrid perovskites exhibit four different crystal symmetries categorized into cubic, tetragonal (I and II) and orthorhombic. Tetragonal and orthorhombic phases are the most common non-cubic perovskite structures characterized by a three-dimensional network of corner-sharing octahedra. In the tetragonal phase only one tilting angle is different from zero, whereas all the tilting angles are nonzero in the orthorhombic phase. The room temperature phase of $MAPbBr_3$ is cubic phase ($\alpha - MAPbBr_3$), with space group $Pm\bar{3}m$. Decreasing temperature, the first phase transition from cubic to tetragonal I ($\alpha - MAPbBr_3$ to $beta - MAPbBr_3$ respectively) takes place at about 236 K, with space group $I4/mcm$. This structure is maintained until the crystal reaches 155 K, at which the second phase transition from tetragonal I to tetragonal II takes place($\beta - MAPbBr_3$ to $\gamma - MAPbBr_3$), space group is $P4/mmm$. Finally, $MAPbBr_3$ is in orthorhombic phase after performing the last phase transition from $\gamma - MAPbBr_3$ to $\delta - MAPbBr_3$ at 149K (space group $Pna2_1$) [2–4]. Temperature regions, space group and lattice constants of four crystalline phases of $MAPbBr_3$ single crystal are listed in Table 1.

	T(K)	Crystalline phase	Space group	Lattice constant (Å)
$\alpha - MAPbBr_3$	>236	Cubic	$Pm3m$	a=5.901
$\beta - MAPbBr_3$	155-236	Tetragonal	$I4/mcm$	a=8.322
				c=11.831
$\gamma - MAPbBr_3$	149-155	Tetragonal	$P4/mmm$	a=5.894
				c=5.861
$\delta - MAPbBr_3$	<149	Orthorhombic	$Pna2_1$	a=7.979
				b=8.580
				c=11.849

Table 1.1: *Temperature regions, space groups, and lattice constant of four $MAPbBr_3$ phases*

In order to anticipate wether the material would arrange in a perovskite structure, in 1926 Goldschmidt proposed the so called tolerance factor (t). It is a relevant structural parameter for expressing the stability of perovskite compounds still used as guiding principle to design hybrid perovskite materials. It is a dimensionless value defined as

$$t = \frac{(r_A + r_X)}{\sqrt{2}(r_B + r_X)} \tag{1.1}$$

where r_A, r_B and r_X are the ionic radii of A, B, X atoms. To understand the meaning of t, consider a unit cell in which the B-site cation is at the center such that there are alternating atomic planes consisting of A-X and B-X atoms (Figure 1.2). In the close pack configuration the diagonal distance from the center of the square to corner is $r_A + r_X$ for the A-X plane and $\sqrt{2}(r_B + r_X)$ for the B-X plane, concluding that the tolerance factor simply represents the ratio of the diagonal distances in the alternating planes.
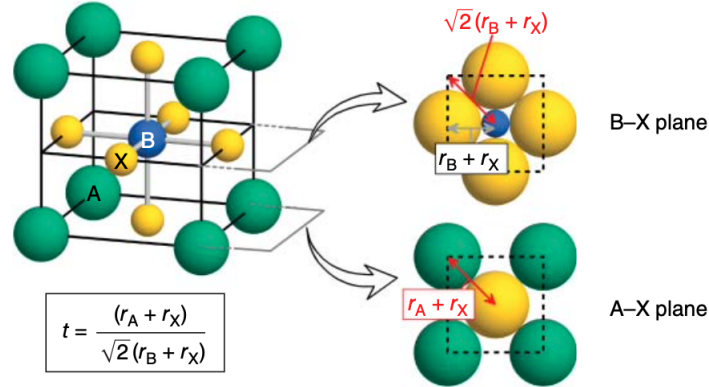

Figure 1.2: *Visual representation of tolerance factor calculation for perovskite structure [5].*

For the calculation of t the actual r_A, r_B and r_X are needed. However, as ions are not rigid spheres and their size depends on the peripheral conditions, the calculation of ionic radii is generally difficult. For instance, r_B changes with the choice of r_X due to the effect of electronegativity, while in the case of organic cation it has non spherical geometry and the hydrogen bonding further varies the bond length, making the determination of r_A difficult. Because of this uncertainty, calculating an accurate t value is a challenging problem. Nonetheless, materials with tolerance factor in the range $0.81 - 1.01$ are considered to adopt a perovskite structure [6]. For further understanding of stability, the octahedral factor μ is defined as

$$\mu = \frac{r_B}{r_X} \tag{1.2}$$

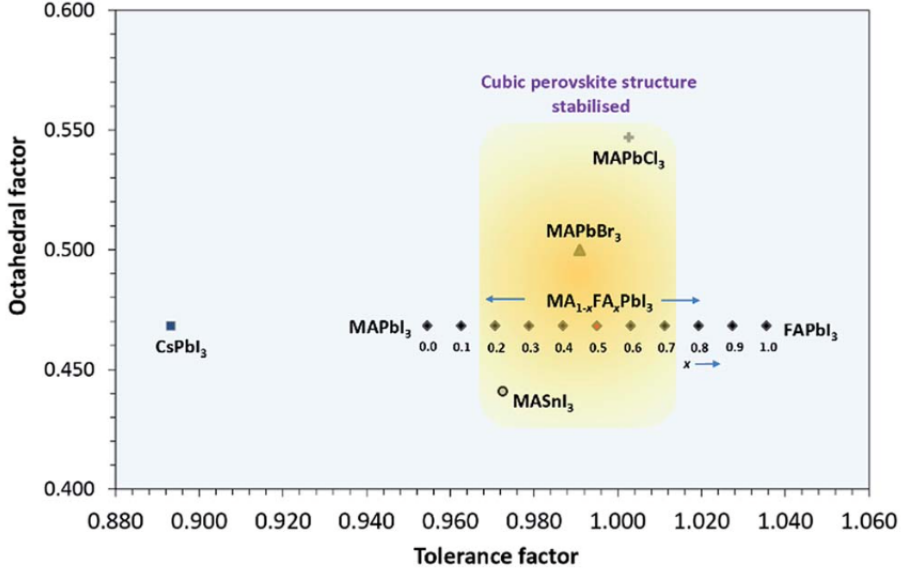In this case, stability is reached for values $\mu > 0.41$.

Figure 1.3: *Octahedral factor vs tolerance factor: range of stability in cubic structure [7].*

Figure 1.3 shows octahedral factor (μ) versus tolerance factor (t).This graph illustrates the range of compositions stabilized in the cubic perovskite structure for hybrid lead halide perovskites (yellow area).

1.2 Optical properties

Since hybrid perovskites comprise an organic cation and inorganic scaffold, these materials benefit of optical characteristics of both organic and inorganic parts. They show unique light absorption properties in a wide energy region extending from 10^{-6} to 6 eV. The band gap of hybrid perovskites is extensively tunable, with light emission ranging

from ultraviolet to near-infrared. This can be achieved following several paths including compositional substitution and dimensionality tailoring. As in standard semiconductors materials, perovskites can be confined to low dimensions including 0D nano crystals (NCs), 1D nanorods and 2D nanosheets. Changing the geometric size of perovskite nanostructures will change the bandgap, so that the bandgap energy of a low-dimensional perovskite will increase compared to the 3D equivalent [8]. An example is shown in Figure 1.4, where photoluminescence emission wavelengths were tuned by the gradual reduction in size of FAPbI3 NCs.
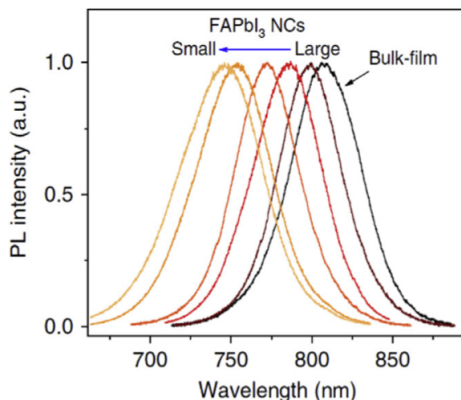

Figure 1.4: *Photoluminescence spectra of* FAPbI$_3$ *nanocrystals of different sizes*

Considering perovskite crystal structure (ABX$_3$), the substitution of the cations (A) and metal (B) can redefine the bandgap of a perovskite and tune the emission spectrum. However the influence of X-site anion is considerably greater than those of A-site and B-site cations (Figure 1.5) [5]. The general trend of energy gap widening with lighter atoms holds, as shown in Figure 1.5(right).
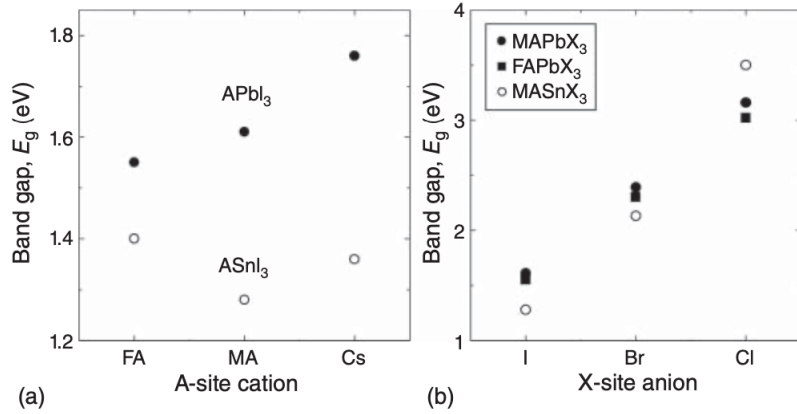
Figure 1.5: *Variation of* E_g *with A cation (left) and X anion (right)*

As a consequence, in $MAPbX_3$ the entire absorption spectrum shifts toward higher energy as the X-site halide anion becomes lighter. This horizontal shift can be explained by applying the sum rule

$$\int E\epsilon_2 dE = const \tag{1.3}$$

where ϵ_2 is the imaginary part of the dielectric constant related to the absorption coefficient through the relation $\alpha = \frac{2\pi\epsilon_2}{n\lambda}$. The sum rule requires that, when the ϵ_2 spectrum is shifted toward a higher energy by ΔE, the ϵ_2 amplitude is reduced by a factor of $f = E/(E + \Delta E)$.

Some of the main charge carrier transport properties are described in the following, with particular attention to MAPbBr$_3$ single crystals.
Under illumination Wannier excitons are generated in hybrid halide perovskites. Excitons are quasiparticles consisting of bound electron-hole pairs, that is capable of carrying energy while being charge neutral. Frenkel excitons are generally found in organic semiconductors, having a binding energy higher than thermal energy($\sim$ 25 meV). Wannier excitons instead are generated in inorganic semiconductors with an exciton binding energy comparable or lower than thermal energy, so they will spontaneously dissociate to generate free charge carriers. In MAPbBr$_3$ single crystals ground state exciton binding energy is found to be 15.33 meV close to 0K, with Bohr radius of $\sim$4.38 nm [9].

1.3 Transport properties

Among charge transport properties, mobility and diffusion length are crucial for detection and photovoltaic application. The charge carrier mobility μ is defined as the drift velocity of the charge carrier $\vec{v_d}$ per unit electric field $\vec{E}$ (Equation 1.4). In general it has different values whether charge carriers are electrons or holes, as it is dependent on the effective mass m^* (Equation 1.5).

$$\vec{v_d} = \mu \vec{E} \tag{1.4}$$

$$\mu = \frac{q\tau}{m^*} \tag{1.5}$$

Time of Flight (ToF) is a widely used experimental method to measure charge carrier mobility in semiconductors. From literature, ToF mobility values of $MAPbBr_3$ single crystals range from 13 to 217 cm^{2}V^{-1}s^{-1} for holes and from 25 to 190 cm^{2}V^{-1}s^{-1} for electrons, showing asymmetric transport properties ($\mu_e\tau_e \ll \mu_h\tau_h$, with τ carrier lifetime) [10]. In this kind of measurement, mobility is derived from the transient time t_t of charge carriers which are photo-generated by a laser pulse. This happens in the immediate vicinity of a semi-transparent electrode, so that only one carrier between holes and electrons contributes to the photocurrent by drifting through the thickness (L) of the sample to reach the opposite electrode. Hence mobility is calculated using

$$\mu = \frac{L^2}{(V * t_t)}(cm^2V^{-1}s^{-1}) \tag{1.6}$$

with an applied voltage V to the sample and an homogeneous electric field.

The second key property is carrier diffusion length L_D, defined as the average distance that a charge carrier travels before recombining

$$L_D = \sqrt{k_B T \frac{\mu\tau}{q}} \tag{1.7}$$

where k_B is the Boltzmann constant, T is temperature and q the elementary charge. In MAPbI$_3$ and MAPbBr$_3$ bulk single crystals diffusion length varies from 1.3 to 175 μm and from 1.8 to 4.3 μm respectively [1].

Despite the advances in the study of perovskites optoelectronic properties, the origin of some of these are still under debate. Ion transport was considered the cause of many important properties of hybrid perovskites (as shown in Figure 1.6), but still the chemical

identity of migrating ions and the transport mechanisms remain unclear, hindering a complete rational design of perovskite optoelectronic devices.
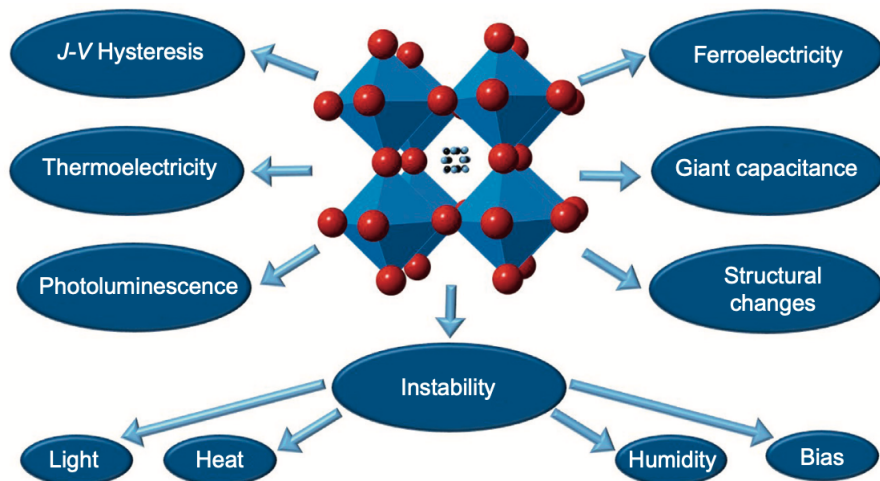

Figure 1.6: *Observed phenomena in hybrid perovskites with possible relationship to ion transport. [11]*

1.3.1 Ion transport

Experimental evidences show that hybrid halide perovskites are ionic semiconductors in which both electronic and ionic transport is possible thanks to the soft ionic crystal structure and ionic conductive properties. Additionally, we have to consider that there are multiple mobile ions in hybrid perovskites, all possibly responsible for experimental observation of ion transport. One of the first experimental evidence was the current-voltage hysteresis of hybrid perovskite solar cells reported by Snaith *et al.* [12] in 2014, as shown in Figure 1.7.
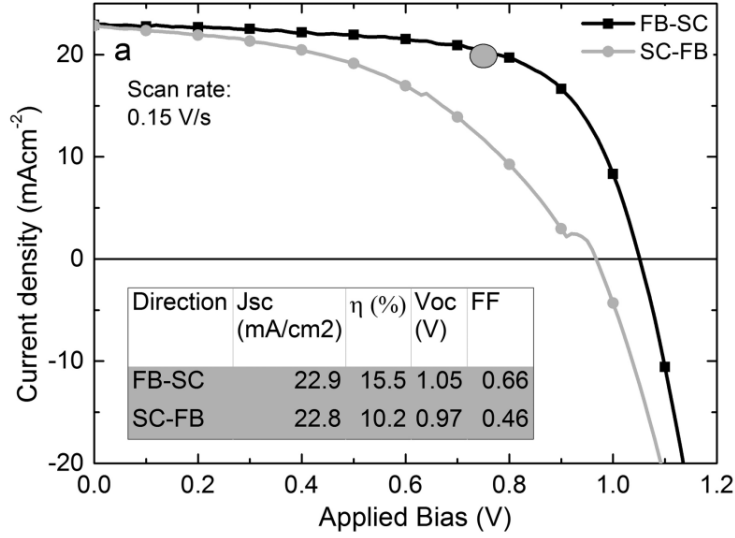
Figure 1.7: *Forward and reverse current-voltage curves measured under AM1.5 simulated sun light for a mesosuperstructure solar cell comprising a mesoporous alumina film coated with a perovskite layer*

Furthermore, hybrid perovskites are relatively unstable materials: they have high and variable defect density and degrade quickly under many device-relevant conditions such as light, heat, humidity and electrical bias [11]. As perovskites are often fabricated by low temperature solution methods, high density of defects is unavoidable (reported to be between 10^{16} and 10^{18} [13]). Thus, ionic defects or vibrational displacements create open spaces for ion migration as they allow ions to move from one location to another. From a thermodynamic and kinetic point of view, an ideal single crystal consists of static atoms at absolute zero, where their potential energy determines the free energy. The kinetic energy contribution of the atomic vibration increases with increasing temperature, with the consequent increase of the free energy of the system. Conversely the system decreases its free energy by increasing the entropy and as a consequence crystal defects arise in the process. Ionic activation energy is defined as the minimum free energy barrier that an ion needs to overcome for it to move from its initial position to adjacent position. Some works have shown that many defects with low activation energy exist in perovskite materials, so that these defects can gain enough energy to migrate under operating conditions such as illumination, electric field and working temperature. We can then state that ion migration is inevitable in hybrid perovskites. As an example in $MaPbI_3$ the constituting ions MA^+, Pb^{2-}, I^- have the potential to migrate and form various defects. Furthermore, the O^{2-} and H^+ captured from the atmosphere have the possibility of ion migration [14].

Generally speaking, activation energy can represent the barrier of ion migration and its

relation with the migration rate is depicted as

$$r_m \propto \exp(-E_A/k_B T) \qquad (1.8)$$

where k_B and T are the Boltzmann constant and temperature. Ion migration rate can also be expressed by the ion diffusion length D_{ion} where

$$D_{ion} = D_0 \exp(-\Delta G_{ion}/k_B T) \qquad (1.9)$$

In this equation D_0 is a temperature dependent factor while the second term represents the probability of an ion overcoming the activation energy barrier for solid state diffusion ΔG_{ion}. On the basis of these equations, it is possible to state that different ions usually have different E_A because this latter is not only related to temperature, but also material structure and the migration distance [14].

Ion migration process is usually carried out by internal defects, including Schottky and Frenkel defects (Figure 1.8 a-b respectively). In addition to that, there are lattice distortions caused by local charge accumulation (Figure1.8c), lattice disorder caused by the dissolution of impurities (Figure 1.9d) and lattice softening due to illumination (Figure 1.9e).
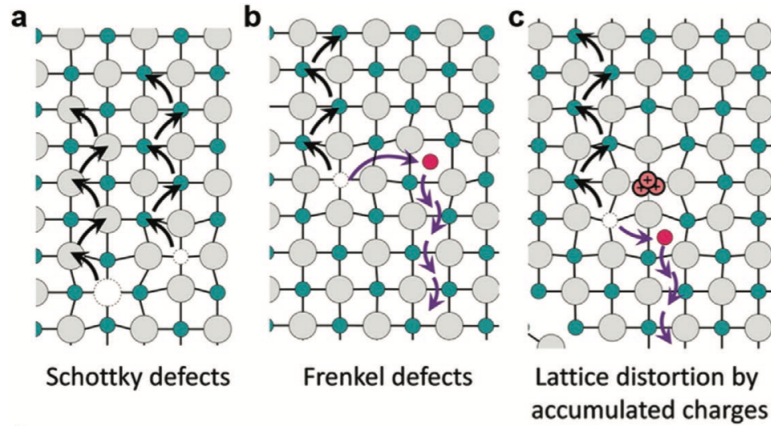

Figure 1.8: *Ion migration channels in hybrid perovskites. a) Schottky defects. b) Frenkel defects. c) Lattice distortion by accumulated charges [15].*
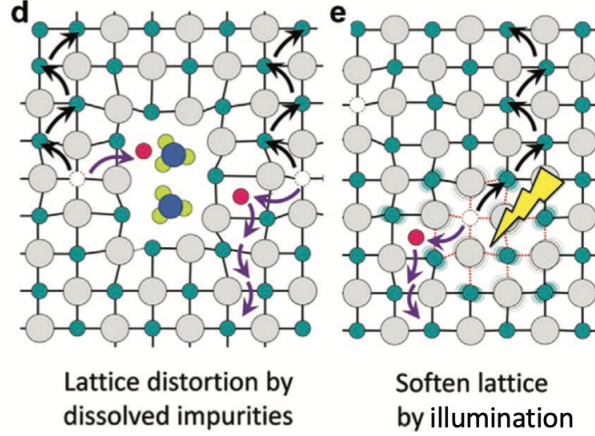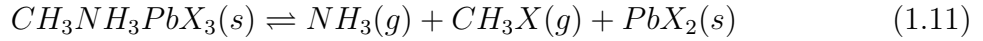
Figure 1.9: *Ion migration channels in hybrid perovskites. d) Lattice distortion by dissolved impurities. e) Softened lattice by illumination [15].*

Ion migration was also accounted for poor stability due to degradation in perovskite devices. The stability of metal halide perovskite is found to be composition dependent: as an example MAPbI₃ is more sensitive to environmental factors, like moisture or temperature, than MAPbBr₃. In terms of degradation, the enhanced stability of MAPbBr₃ is connected to a predominance of the reversible decomposition reaction

$$CH_3NH_3PbX_3(s) \rightleftharpoons CH_3NH_2(g) + HX(g) + PbX_2(s) \qquad (1.10)$$
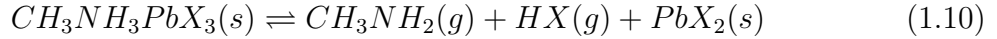
compared to the irreversible decomposition pathway

$$CH_3NH_3PbX_3(s) \rightleftharpoons NH_3(g) + CH_3X(g) + PbX_2(s) \qquad (1.11)$$

in contrast to MAPbI₃ that exhibits both types of decomposition. In terms of ion migration, McGovern *et al.* [16] found that, in contrast to theoretical predictions for MAPbBr₃ that suggest stronger Pb-Br bond which could increase the halide ion defect formation energy suppressing the degradation due to ion migration, the activation energy of bromine is reduced with respect to iodine. However despite the reduced activation energy, halide diffusion is slower presumably because of a lower entropic change for ion migration. They also showed that bromine substitution inhibits MA$^+$ ion migration due to lattice contraction [16].

1.4   Stability issues

As mentioned above, ion migration is one of the causes for perovskites instability. This mechanism is regarded as intrinsic instability, to be differentiated from environmental instability due to external stimuli like moisture, oxygen, light and heat. Methylammo-

nium lead iodide can be taken as an example to illustrate perovskite chemical stability.

Water is known to be extremely detrimental for perovskite materials, as prolonged exposure to water vapor triggers irreversible material degradation, leading to the conversion of perovskite into its precursors. Specifically for MAPbI$_3$, water forms hydrate complexes as $(CH_3NH_3)_4PbI_6 \cdot 2H_2O$, with PbI$_2$ that tends to crystallize. Moreover MA$^+$ is slightly acidic and reacts with water to form volatile methylamine and hydroiodic acid following the reaction

$$(CH_3NH_3)_4PbI_6 \cdot 2H_2O \rightarrow PbI_2 + 4CH_3NH_3 + 4HI + 2H_2O \qquad (1.12)$$

Similar reaction occurs for MAPbBr$_3$ reaction with water. A macroscopic change can be noticed as crystal is clear and shiny before water exposure but looses its transparency and mirrorlike surface afterward. The color also changes from dark red to light orange as shown in Figure 1.10 [17]
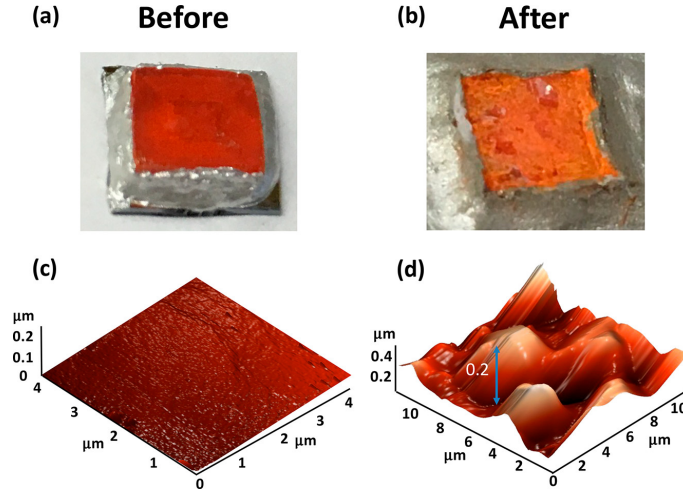

Figure 1.10: *MAPbBr$_3$ single crystal (a) before and (b) after water exposure. Three-dimensional AFM images of the crystal surface (c) before and (d) after water exposure.*

Temperature is another factor affecting perovskite stability. For example MAPbI$_3$ is intrinsically unstable upon thermal stress that induces a released of I$_2$ and the appearance of metallic Pb at about $40°C$ without any illumination source. This is due to the following decomposition reactions:

$$CH_3NH_3PbI_3 \rightarrow CH_3NH_3I + PbI_2 \qquad (1.13)$$

$$PbI_2 \rightarrow Pb0(s) + I_2(g) \qquad (1.14)$$
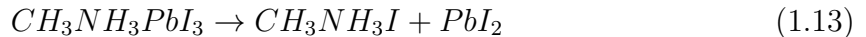
Also oxygen and light can alter perovskite stability as metal halide perovskites are highly prone to photo-oxidation. In MAPbI$_3$ oxygen starts diffusing almost instantaneously upon illumination and the decomposition is completed within an hour. In this process oxygen absorbs and diffuses through iodide vacancies [18].

1.5 Applications

Despite the simplicity of the original perovskite crystal structure, this family shows an impressive variety of compounds. Moreover, depending on which atoms and/or molecules are involved, perovskites have a remarkable array of interesting properties, making them an exciting playground for studying optoelectronic properties of complex materials. Because of this nature, perovskites have been used in a variety of different applications. Beyond any doubt, the most popular application of perovskite compounds is in photovoltaic technology, followed by ionizing radiation detection and LEDs architectures.

1.5.1 Solar cells

Perovskite solar cell is a general definition used to identify a large variety of devices employing perovskites as light absorbing layer stacked between selective layers and contacts. Perovskite fame as promising material was largely due to the steep increase of power conversion efficiency (PCE) from 3% to over 25% in no more than ten years [19]. The first work demonstrating an operating perovskite based solar cell was published in 2009 by Kojima *et al.* [20]. In this innovative work the authors employed $CH_3NH_3PbI_3$ as sensitizer in a Dye-Sensitized-Solar-Cell (DSSC) like device, where perovskite was deposited on a mesoporous TiO$_2$ layer. The stability of such device was rather poor because of the degradation of perovskite material into the liquid electrolyte hole transporting material. In 2012 perovskite solar cells performed a step forward as Lee *et al.* [21] and Kim *et al.* [22] reported independently a PCE over 9%, using solid state hole selective contact in replace of liquid electrolyte. From there on, the fast increase of PCE was down to the advancement in both compositional and architecture engineering.
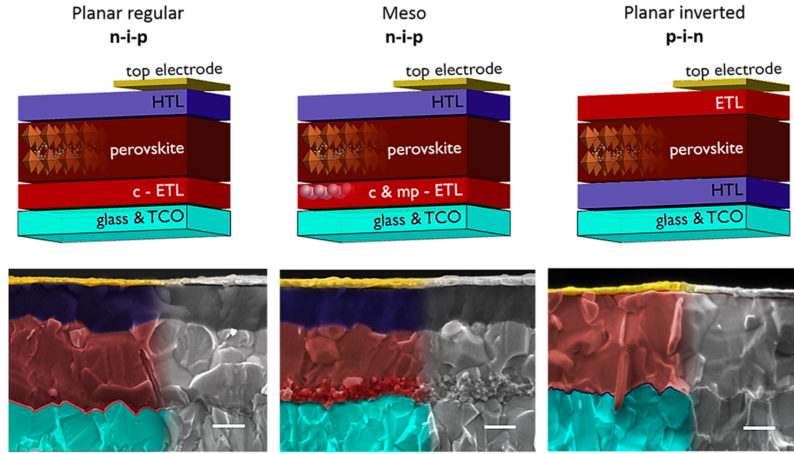
Figure 1.11: *Top images: schematics of planar regular (n-i-p), mesoporous (n-i-p), and planar inverted (p-i-n) architectures respectively. The device is composed of a transparent conductive oxide (TCO) on top of a glass substrate, a compact and mesoporous electron transporting layer (c & mp - ETL), a hole transporting layer (HTL), the perovskite, and the top electrode. Bottom images: SEM cross-section images of representative devices with scale bar of 200nm [23].*

1.5.2   Radiation detectors

Currently used radiation detectors are based on inorganic semiconducting materials as silicon, cadmium telluride (CdTe) and cadmium zinc telluride (CZT). Although these materials exhibit impressive detection performances, there are some drawbacks limiting their operation as difficulty to grown large area high quality low cost crystals and the difficulty to process them into pixelated detector matrices on flexible substrates. The unique properties that made perovskites promising materials for efficient solar cell applications like tunable band gap, large mobility, long carrier recombination lifetime, are actually also desirable for radiation detection. The typical $MAPbI_3$ halide perovskite has a density of around 4g/cm^3, providing a large linear attenuation coefficient of $10cm^{-1}$ to 100 keV, which is comparable to that of CZT material [24]. Moreover the possibility to form more complex compounds, such as Cs_2AgBiI_6 quasi-perovskite , allows the incorporation of many other high Z elements into the structure. The mobility and charge recombination lifetime measurements on $MAPbI_3$ show a large $\mu\tau$ product of the order of $10^{-2}cm^2V-1$ corresponding to long diffusion length on the order of micrometers [24]. Another important figure of merit in radiation detection is the bulk resistivity of the semiconductor, in order to have small dark current and low noise. Resistivity value measured for $MaPbI_3$ is of the order of $10^7\Omega cm$ at room temperature, while in $MAPbBr_3$ can be ten times higher. While in inorganic semiconductors resistivity can reach up tp 10^{10} Ωcm, satisfying the requirement for γ-ray spectroscopy, they have low values of $\mu\tau$

product. Usually MAPbBr$_3$ is used in the photoconductor device architecture. These latter are 2-terminal architectures where the absorbing material is stacked between two conductive electrodes. The device geometry can be either vertical (Figure 1.12a), in which the absorbing layer is sandwiched between the electrodes, or co-planar (Figure 1.12b), where the active layer is directly exposed to radiation and laterally interfaced with contacts.
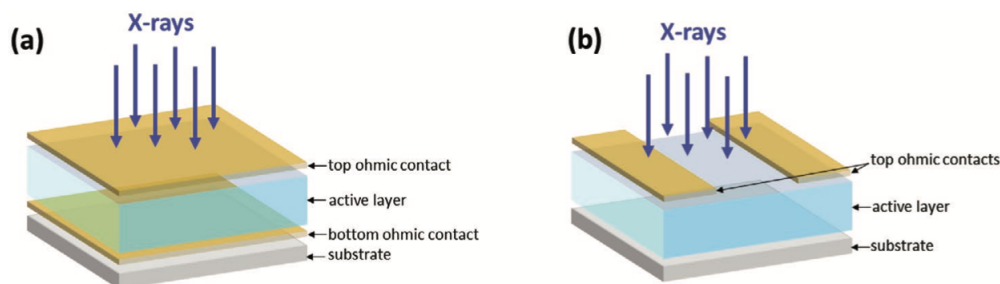

Figure 1.12: *Schematics of photoconductor architectures for direct X-ray detection. a) Vertical photoconductor architecture; b) co-planar photoconductor architecture [24].*

1.5.3 LEDs

Beyond solar cell applications, hybrid metal halide perovskites proved to be promising materials to be applied in LEDs thanks to their excellent color purity, tunable band gap, high charge mobility and excellent photoluminescence quantum efficiency (PLQE) [25]. Hybrid halide perovskite Quantum Dots (QD) are especially suited for LED application because of their unique characteristics of high brightness and narrow-band photoluminescence (PL). Moreover, perovskite QDs exhibit a high PLQE even close to 100% owing to the outstanding quantum confinement effect and show tunable optical properties, as the luminescence colour of the perovskite QDs-based LEDs can be tuned from ultraviolet (UV) to near-infrared (NIR) wavelength region through simple management of QD sizes or halide compositions.

As illustrated before, hybrid halide perovskites materials have a wide range of applications as a result of their outstanding properties. Because of this, the study of such materials is a significant task in order to go past "state of art" devices. Among the remaining issues to be solved, defects characterization is one of the most compelling and it is relevant to all the above mentioned applications. Actually, defects can decrease charge collection efficiency in solar cells and detectors, they can act as dopants, increasing the material resistivity leading to higher dark current which is detrimental for radiation detection and they can serve as non-radiative recombination centers, which is damaging for LED technology.

Chapter 2

Impurity and defect states in semiconductors

As mentioned in Chapter 1, methylammonium lead halide perovskites are promising materials with unique optoelectronic properties. However two main issues remain to be solved: stability and defect control. As defects affect the charge transport properties, the understanding of their nature and energy scale is therefore crucial for the development and optimization of perovskites based devices. Having information on defects parameters is the key to design defect control strategies and to understand the impact that defects play on stability and transport properties.

Impurities and defects can be classified into deep and shallow. Shallow states are considered as substitutional hydrogenic impurities at which the electron is bounded by Coulomb interaction. On the other hand, in deep states the impurity potential is strongly localized so that electrons are tightly bound. This results in an energy level of deep states that is closer to the center of the energy gap of the material. Conventionally, a defect is regarded as deep if its position is deeper than the thermal energy at room temperature ($2 \cdot k_B T = 0.05 eV$) from the band edges [26]. As some material properties can be controlled by small concentrations of these centers, the study of deep states require measurement techniques sensitive to low concentrations of such deep states in presence of much greater concentration of shallow impurities. These techniques are related to the observation of transient phenomena, where the transient time constant provides information about the rate of capture and emission processes at deep states.

2.1 Physical principles for studying deep states with transient measurement techniques

Rate equations relate the rate of change of electron and hole occupancy of the trap to capture and emission processes.

Consider n free electrons per unit volume moving with thermal velocity $<v_n>$ so that a deep state is exposed to a flux of $n<v_n>$ electrons per unite area per unit time. As the total concentration of deep centers is N_t, if at any instant n_t of these are occupied by electrons the number of electron captured by $(N_t\text{-}n_t)$ unoccupied states in a time interval Δt is

$$\Delta n_t = \sigma_n <v_n> n(N_t - n_t)\Delta t \tag{2.1}$$

where σ_n is the capture cross section characterizing the capture process. The capture rate per unoccupied sate is defined as

$$c_n = \frac{(\Delta n_t / \Delta t)}{(N_t - n_t))} \tag{2.2}$$

hence, substituting is

$$c_n = \sigma_n <v_n> n \tag{2.3}$$

A similar equation can be obtained for capture rate of holes in occupied states

$$c_p = \frac{(\Delta(N_t - n_t)/(\Delta t)}{n_t} = \sigma_p <v_p> p \tag{2.4}$$

State occupancy is determined by the competing emission and capture processes: electrons are emitted and holes captured at the n_t states occupied by electrons, while holes are emitted and electrons captured at the $N_t - n_t$ unoccupied states. The net rate of change of electron occupancy is

$$\frac{\mathrm{d}n_t}{\mathrm{d}t} = (c_n + e_p)(N_t - n_t) - (e_n + c_p)n_t \tag{2.5}$$

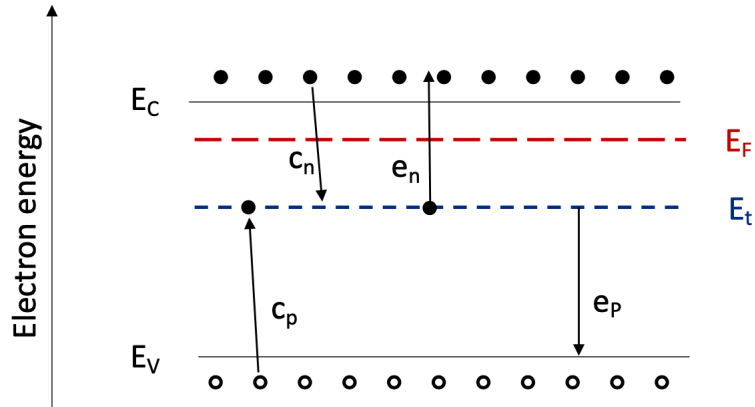where e_n and e_p are the emission rates for electrons and holes respectively.

Figure 2.1: *Electron and hole capture and emission processes for a trap with energy E_t.*

2.1.1 Deep states in thermal equilibrium

In thermal equilibrium, in addition to the steady state requirement $dn_t/dt=0$, capture and emission processes must satisfy the principle of detailed balance. This latter states that the rates for a process and its inverse must be equal and balanced in detail. This principle applied to our system imply that the emission and capture rates of electrons (and holes) must be equal. Without this condition there would be a net transfer of one band to the other while trap occupancy remained in steady state. This condition requires that both

$$e_n n_t = c_n (N_t - n_t) \tag{2.6}$$

and

$$e_p (N_t - n_t) = c_p n_t \tag{2.7}$$

so that thermal equilibrium occupancy of the trap is

$$\frac{\hat{n}_t}{N_t} = \frac{c_n}{c_n + e_n} = \frac{e_p}{e_p + c_p} \tag{2.8}$$

In thermal equilibrium the occupancy is also defined by Fermi-Dirac distribution function. Consider a system with Fermi energy E_F, for a deep state at energy E_t with degeneracy g_0 when unoccupied and g_1 when occupied by one electron, the occupancy is

$$\frac{\hat{n}_t}{N_t} = \{1 + \frac{g_0}{g_1} \exp\left(\frac{E_t - E_F}{kT}\right)\}^{-1} \tag{2.9}$$

Combining equation 2.9 and equation 2.8 gives

$$\frac{e_n}{c_n} = \frac{g_0}{g_1} \exp\left(\frac{E_t - E_F}{kT}\right) \tag{2.10}$$

for electron emission, while for hole emission

$$\frac{e_p}{c_p} = \frac{g_1}{g_0} \exp\left(\frac{E_F - E_t}{kT}\right) \tag{2.11}$$

Seeing that $(g_1/g_0) \approx 1$, these equation show that when the Fermi energy is above the trap energy E_t the electron capture rate is greater than the emission rate and the holes emission rate is greater than the capture rate ($c_n > e_n$ and $e_p > c_p$) so the state is occupied with electrons. On the other hand when Fermi energy is below E_t, $e_n > c_n$ and $c_p > e_p$ resulting in an empty state.

The different relative magnitudes of the emission and capture rates with respect to the Fermi energy for electrons and holes is related to the fact that capture rates are determined by the free carrier concentration (Equations 2.2 and 2.3). For a non degenerate semiconductor (with a moderate level of doping)

$$n = N_c \exp\left(-\frac{E_c - E_F}{kT}\right) \tag{2.12}$$

hence, when the Fermi energy is near the band edge and above E_t, the electron capture rate c_n is large while, if it is below E_t, n and c_n are small. Notice that capture rates are dependent on the sample doping while capture cross section and emission rate are intrinsic properties of the deep state.

At equilibrium it is possible to obtain the electron emission rate substituting Equations 2.3 and 2.12 into 2.11

$$e_n(T) = \sigma_n < v_n > \frac{g_0}{g_1} N_c \exp\left(-\frac{E_c - E_t}{kT}\right) \tag{2.13}$$

Likewise for holes we obtain

$$e_p(T) = \sigma_p < v_p > \frac{g_1}{g_0} N_v \exp\left(-\frac{E_t - E_v}{kT}\right) \tag{2.14}$$

These equations describe the emission rates in terms of capture cross sections and energy separations of the energy level of the trap from the appropriate band edge. This means that these properties are not independent and can be considered primary properties of the trap.

The temperature dependence of the emission rate can be calculated considering the electron case as an example: we have

$$< v_n > = \left(\frac{3kT}{m^*}\right)^{\frac{1}{2}} \tag{2.15}$$

and

$$N_c = 2M_c \left(\frac{2\pi m^* kT}{h^2}\right)^{\frac{3}{2}} \tag{2.16}$$

where M_c is the number of conduction minima. We allow for a temperature-dependent capture cross section of the form

$$\sigma(T) = \sigma_\infty \exp\left(-\frac{\Delta E_\sigma}{kT}\right) \tag{2.17}$$

where σ_∞ is the capture cross section at T=∞. Substituting this into Equation 2.13 we obtain the temperature dependence of the electron emission rate $e_n(T)$

$$e_n = \gamma T^2 \sigma_{na} \exp\left(-\frac{E_{na}}{kT}\right) \tag{2.18}$$

in which

$$\gamma = 2\sqrt{3}M_c(2\pi)^{\frac{3}{2}}k^2m^*h^{-3} \tag{2.19}$$

and

$$\sigma_{na} = \frac{g_0}{g_1}\sigma_\infty \tag{2.20}$$

where σ_{na} is defined as the apparent capture cross section.

Therefore, plotting $\ln(T^2/e_n)$ as a function of T^{-1} results in a straight line characterized by slope equal to the activation energy E_{na} and intercept as σ_{na}. This is commonly known as Arrhenius plot, producing a trap signature which can be used to compare and identify these species. It is important to highlight that in this formulation E_{na} can be identified with $(E_c - E_t) + \Delta E_\sigma$, hence it does not give the energy level of the trap directly. Moreover, both E_{na} and σ_{na} definitions hold if $(E_c - E_t)$ is temperature independent.

In the typical construction of energy band diagrams of semiconductors the energy band gap represents the minimum energy necessary to excite an electron from the valence band to the conduction band. This concept holds when we interpret optical measurements performed at constant temperature. However, in many electrical experiments temperature change is necessary to cause an alteration of a measurable property, leading to a change in the band gap due to temperature variation during the experiment. In view of this, by interpreting measurements of thermal emission rate as a function of temperature we need to consider that one or both the energy separation being measured $(E_c - E_t)$ and $(E_t - E_v)$ change with temperature. It is necessary to look deeply into the definition of the energy band gap in a semiconductor which is defined as the sum of chemical potentials for the formation of electron and hole pairs [27]. Accordingly the energy level of a trap state is defined as the change in chemical potential for the formation of a free carrier and an ionized defect. The chemical potential is defined as the increase of Gibbs free energy G per electron-hole pair or carrier ionized defect pair, at constant temperature and pressure, so the band diagram can be interpreted as representing the Gibbs free energies for the appropriate particle pair. Using these definitions the thermal emission rate of carrier from a deep state at temperature T is defined as

$$e_n(T) = \sigma_n(T) < v_n(T) > N_c(T)exp(-\frac{\Delta G(T)}{kT}) \tag{2.21}$$

where $\Delta G(T)$ is the Gibbs free energy change for ionization of the state. $\Delta G(T)$ is equal to the separation of the energy level of the state from the appropriate band edge at temperature T, that for electron is

$$\Delta G(T) = E_c(T) - E_t(T) \tag{2.22}$$

26

The thermodynamic identity $\Delta G(T) = \Delta H - T\Delta S$ relates the Gibbs free energy change to the associated changes of enthalpy and entropy, so we can rewrite Equation 2.21 as

$$e_n = \chi_n N_c(T)\sigma_n(T) < v_n(T) > \exp\left(-\frac{\Delta H}{kT}\right) \qquad (2.23)$$

where

$$\chi_n = \exp\left(\frac{\Delta S}{k}\right) \qquad (2.24)$$

Considering for the moment a temperature independent cross section, Equation 2.23 shows that plotting T^2/e_n as a function of T^{-1} results in a line with slope characterized by the enthalpy ΔH. Usually ΔH is weakly dependent on temperature so this slope is an average of the change in enthalpy over the temperature range of the plot. As $\Delta H(T)$ is different from $\Delta G(T) = E_c(T) - E_t(T)$, the slope of the Arrhenius plot is different from the threshold photon energy in an isothermal optical experiment.

2.1.2   Transient response

The general rate of change of electron occupancy can be rewritten as

$$\frac{dn_t}{dt} = a(N_c - n_t) - bn_t \qquad (2.25)$$

where a and b coefficients are defined as

$$a = \sum \text{rates of "electron gain"} (c_n + e_p) \qquad (2.26)$$

$$b = \sum \text{rates of "electron loss"} (e_n + c_p) \qquad (2.27)$$

Now, if $n_t = N_t(0)$ when t=0, the general solution of Equation 2.25 is

$$n_t(t) = \frac{a}{a+b}N_t - \left\{\frac{a}{a+b}N_t - n_t(0)\right\}\exp[-(a+b)t] \qquad (2.28)$$

and the steady state occupancy is given by setting $t = \infty$ or equivalently setting Equation 2.25 equal to zero, obtaining

$$n_t(\infty) = \frac{a}{a+b}N_t \qquad (2.29)$$

In general we can write

$$n_t(t) = n_t(\infty) - n_t(\infty) - n_t(0)\exp(-t/\tau) \qquad (2.30)$$

where τ is the time constant given by

$$\tau^{-1} = (a+b) = e_n + c_n + e_p + c_p \qquad (2.31)$$

The general solution of Equation 2.25, Equation 2.28 explains that if the occupancy is momentarily perturbed from $n_t(\infty)$ to $n_t(0)$ it then relaxes exponentially to the steady state occupancy with a rate constant being the sum of the rates of all the operative processes (emission and capture). On the relative magnitude of $n_t(\infty)$ and $n_t(0)$, namely whether $n_t(0)$ is greater or less than $n_t(\infty)$ depends the meaning of this relaxation (Equation 2.30). The initial occupancy is set by experimental conditions. However there are two limiting situation frequently encountered, fully occupied state and empty state. When the state is initially occupied so $n_t(0) = N_t$, the rate of change decays as

$$n_t(t) = \frac{a}{a+b}N_t + \frac{b}{a+b}N_t \exp[-(a+b)t] \tag{2.32}$$

while when the state is initially empty $n_t(0)$ increases with time as

$$n_t(t) = \frac{a}{a+b}N_t\{1 - \exp[-(a+b)t]\} \tag{2.33}$$

Lastly, we introduce the concepts of majority and minority carrier traps. Electron and hole emission rate equations (2.13 and 2.14 respectively) illustrate that states in the upper half of the gap have $e_n > e_p$ as $(E_c - E_t) < (E_t - E_v)$, while states in the lower half of the gap have $e_p > e_n$. The separation between these two regimes is set for a trap level $E_t = E_1$ for which $e_n = e_p$, given that

$$E_1 = E_i + \frac{kT}{2}\ln\{\frac{\sigma_p < v_p > g_1/g_0}{\sigma_n < v_n > g_0/g_1}\} \tag{2.34}$$

where E_i is the Fermi level position in intrinsic materials

$$E_i = (\frac{E_c + E_v}{2}) + \frac{kT}{2}\ln\left(\frac{N_v}{N_c}\right) \tag{2.35}$$

From now on states in the upper half of the band $(E_t > E_1)$ with $e_n > e_p$ will be addressed as "electron traps", whereas "hole traps" will be those in the lower half of the band gap with $E_t < E_1$ and $e_p > e_n$.

2.2 Photo-induced current transient spectroscopy: PICTS

One of the best known and most used technique for trap characterization is the Deep Level Transient Spectroscopy (DLTS). In this experimental method the sample under study is a diode on which a pulsed bias is applied in order to fill the traps. The resulting series of capacity transients are then processed to generate a spectrum as the sample is slowly heated. The appliance of DLTS is strictly related to the relative concentration

between the free carriers and the traps as, if $n \gg N_T$ in n-type material (or $p \gg N_T$ in p-type material) the capacitive signal of DLTS is high enough to give reliable information. On the contrary, if the resistivity of studied material is high ($> 10^5 \Omega cm$), the concentration of traps can be even orders of magnitude higher than the free carrier concentration leading to a very small capacitive signal, of the order of electric noise [28].
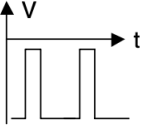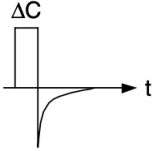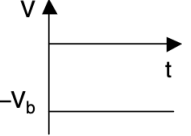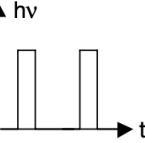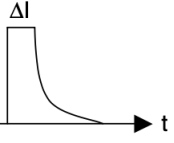

Figure 2.2: *Schematic comparison of operation modes of Deep Levels Transient Spectroscopy (DLTS) and Photo Induced Current Transient Spectroscopy (PICTS).*

In this work DLTS was not applicable as MAPbBr$_3$ is an high resistivity material. For this reason, we performed Photo Induced Current Transient Spectroscopy (PICTS) studies. In this technique trap filling processes are photogenerated by light pulses with energy greater than the band gap. Excess electrons and holes are captured by trap states and subsequently released by thermal emission when light is turned off producing a current transient: light is turned on to generate electron-hole pairs filling the traps with time constant $\approx (c_n + c_p)^{-1}$. When light is switched off photocurrent decays rapidly from its steady state value under illumination, revealing an exponential thermal emission transient.
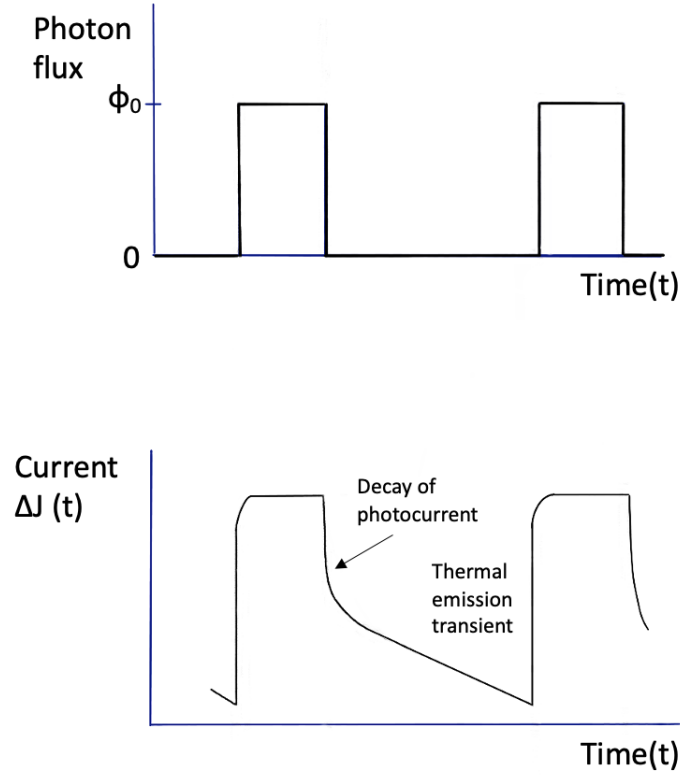
Figure 2.3: *Scheme of photocurrent response to a pulsed light in PICTS experiment.*

Illuminating a semiconductor with a flux Φ_0 generates free electron-hole pairs at a rate G(x) defined as

$$G(x) = (1 - R)\alpha(h\nu)\Phi_0 \exp\{-\alpha(h\nu)x\} \qquad (2.36)$$

depending on the optical absorption coefficient $\alpha(h\nu)$, the distance below the surface of the sample x and the surface reflectivity (R). In direct band gap semiconductors $\alpha \approx 10^5 cm^{-1}$ for $h\nu > E_g$, hence carriers are generated over a distance of a few microns below the surface.

As aforementioned, the effect of illumination is to produce excess electrons and holes that can eventually be trapped at deep states at rates given by

$$c_n = \sigma_n < v_n > \Delta n \qquad (\Delta n \gg n_0) c_p = \sigma_p < v_p > \Delta p \qquad (\Delta p \gg n_0) \qquad (2.37)$$

To induce significant changes in trap occupancy it is necessary that Φ_0 is sufficiently great that c_n and c_p exceed thermal emission rates. Consider a trap in the upper half of the band gap , being above the Fermi level and therefore empty at equilibrium. The electron concentration n_t on these traps increases with time due to capture of photogenerated

carriers. A steady state is reached after a time $\approx (c_n + c_p)^{-1}$ when the occupancy is

$$n_t^{ph}(\infty) = \frac{\sigma_n <v_n> \Delta n}{\sigma_n <v_n> \Delta n + \sigma_p <v_p> \Delta p} \cdot N_t \tag{2.38}$$

and when $\Delta n = \Delta p$ this becomes

$$\frac{n_t^{ph}}{N_t} = \frac{\sigma_n <v_n>}{\sigma_n <v_n> + \sigma_p <v_p>} \approx (1 + \frac{\sigma_n}{\sigma_p})^{-1} \tag{2.39}$$

In these conditions the steady state occupancy reaches a saturation value independent on Φ_0 and dependent only on(σ_n/σ_p). However the time taken to reach the steady state decreases with increasing flux as the rates increase.

After filling the traps, light is turned off and the excess carrier populations in the band decays rapidly at a rate determined by the carrier lifetimes. Once the current is decayed, a transient current remains due to slower thermal emission of trapped carriers from deep states. Considering a sample with ohmic contacts the resulting current transient is exponential under precise conditions:

- retrapping can be neglected;

- the effective recombination rate much faster than thermal emission rate;

- effective recombination rate is itself independent of n_t.

Once these conditions are fulfilled the current transient is given by

$$\Delta J_c(t) = -e\vec{E}\tau_n\mu_n e_n n_t(0) \exp(-e_n t) \tag{2.40}$$

where $\vec{E}\tau_n\mu_n$ is the distance the carrier drifts in the field $\vec{E}$ before recombining. Now assuming that the light pulse is long enough to reach the steady state during the filling period, then $n_t(0)$ is given by $n_t^{ph}(\infty)$ defined in Equation 2.38.
In the case of sandwich configuration of the electrical ohmic contacts, depending on the polarity of the applied bias, either holes or electrons will be injected in the material bulk. As shown in Figure 2.4a, a positive bias applied to the top illuminated electrode will inject only holes into the bulk, leading to a transient current due to de-trapped holes. Vice versa, a negative bias applied to the top electrode will produce a transient current due to de-trapped electrons (Figure 2.4b) [29].
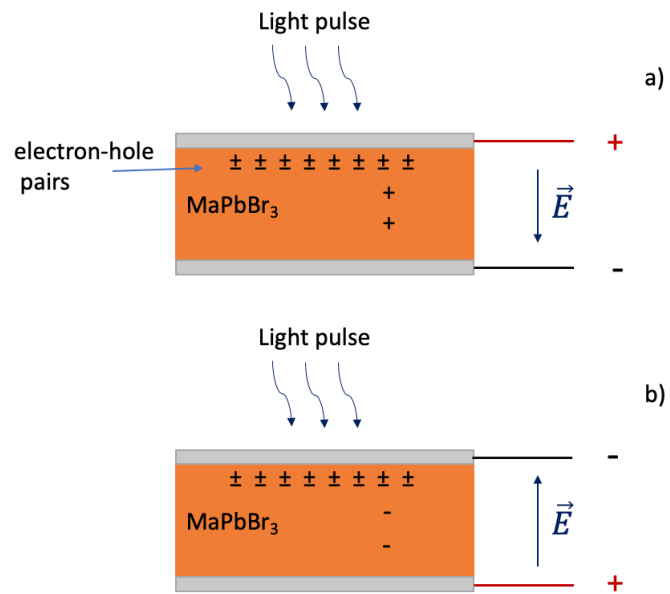
Figure 2.4: *Schematic representation of carrier injection into the bulk of a semiconductor under the influence of an applied field. a) hole injection; b) electron injection.*

Chapter 3

Methods

3.1 MAPbBr$_3$ single crystal synthesis

3.1.1 Inverse temperature crystallization (ITC) method

Firstly developed by Saidaminov *et al.* [30], inverse temperature crystallization (ITC) growth method permits rapid solution growth of high quality, size and shape controlled single crystals, exploiting the loss of solubility occurring in specific solvents at relatively high temperatures known as retrograde solubility.

Generally, solutes tend to have higher degree of solubility at higher temperatures so that a good solvent for crystallization will dissolve more precursors when hot, while cooling down induces supersaturation starting crystallization. Conversely, a decrease of solute solubility in solvents with increasing temperature is an unusual occurrence only exhibited by few materials. Among these latter, MAPbBr$_3$ shows inverse temperature solubility behavior in N,N-dimetilformammide (DMF), while no precipitates where observed in other commonly used solvents like DMSO or GBL. Saidaminov *et al.* noticed that individual precursors lead bromide (PbBr$_2$) and methyl-ammonium bromide (MABr) did not show any inverse solubility behavior , suggesting that this phenomenon is connected to the perovskite structure.

In ITC growth method, MABr and PbBr$_2$ precursors are dissolved at 1:1 molar ratio in DMF in order to obtain 1M solution of MAPbBr$_3$. This solution is then abruptly brought up to 85° from room temperature, leading to spontaneous nucleation and crystal growth as shown in Figure 3.1.
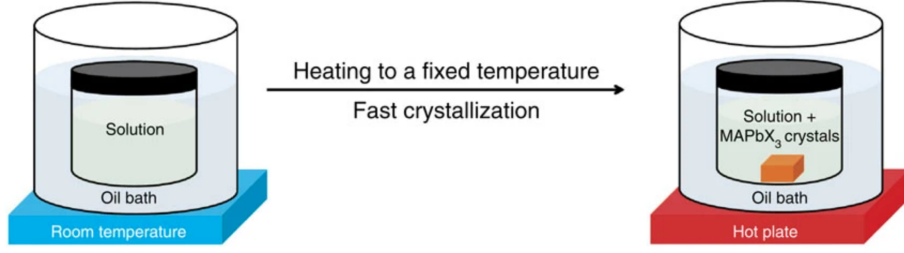
Figure 3.1: *Schematic representation of ITC set-up: the crystallization vial is immersed in an oil bath heated from room temperature and kept at 80° to start the crystallization.*

It is experimentally observed that perovskite crystals formed in precursors solution at elevated temperatures dissolve back when the solution is cooled down to room temperature. This observation indicates that the thermodynamic stability of a precipitated hybrid perovskite compound has unusual temperature dependence, as simple monomolecular compounds are likely to dissolve at higher temperatures. Suppose there is only one type of molecular precursor controlling the crystallization of a complex compound such as perovskite: the formation of complexes involving the precursor molecule and solvent molecule may significantly affect the precipitation of the compound. To understand this situation we have to study the thermodynamic stability of a monomolecular precipitate made of molecules A in the solution, in which A molecules can form complexes with solvent molecules [30]. We assume that the final stable state always contains only one spherical precipitated particle placed in a unit volume of solution.

Consider the Gibbs free energy of a system of unit volume containing n_s solvent molecules in the solution, n_A isolated A-molecules and n_c complexes

$$
\begin{aligned}
G = &- \epsilon n_p + \gamma \cdot S_P - \epsilon_c \cdot n_c + T n_c \cdot \ln(n_c \nu_c) + T n_A \cdot \ln(n_A \nu_A) + T n_s \cdot \ln(n_S \nu_s) \\
&- T \cdot (n_A + n_S + n_C) \cdot \ln(n_A \nu_A + n_s \nu_s + n_c \nu_c)
\end{aligned}
\tag{3.1}
$$

where ϵ is the cohesive energy of A-molecule in the particle, ϵ_c is the complexes binding energy, γ is the surface energy per molecule, S_P is the number of A-molecules on the surface of A-particle, T is the solution temperature and ν_S, ν_C and ν_A are the characteristic volumes of the solvent molecule, the complex and the A-molecule, respectively. It is more convenient to rewrite the Equation 3.1 in terms of total concentrations of A-molecules $m_A = n_A + n_P + n_C$ and solvent molecules $m_S = n_S + j \cdot n_C$, where j is the number of solvent molecules in the A-solvent complex:

$$G = - \epsilon n_p + \gamma \cdot S_P - \epsilon_c \cdot n_c + T n_c \cdot \ln(n_c \nu_c)$$
$$+ T(m_A - n_P - n_C) \cdot \ln((m_A - n_P - n_C)\nu_A) + T(m_S - jn_C) \cdot \ln((m_S - jn_C)\nu_s)$$
$$- T(m_A + m_S - n_P - jn_C) \cdot \ln(\nu_A m_A + \nu_S m_S - \nu_A n_P + n_C \cdot (\nu_C - \nu_A - j\nu_S)) \tag{3.2}$$

Since we are interested in equilibrium size of A-particles and concentration n_C of A complexes with solvent , we choose n_P and n_C as independent variables. Minimizing the free energy with respect to these latter we obtain

$$\frac{\partial G}{\partial n_P} = -\epsilon + \gamma \cdot \frac{2}{R} - T \cdot \ln(n_A \nu_A) = 0 \tag{3.3}$$

$$\frac{\partial G}{\partial n_C} = -\epsilon_C + T \cdot \ln(n_C \nu_C) - T \cdot \ln(n_A \nu_A) - jT \cdot \ln(n_S \nu_S) = 0 \tag{3.4}$$

where R is the particle radius.

Equation 3.3 gives an equality of the chemical potentials in the particle $\mu_{AP} = -\epsilon + 2\gamma/R$ and in the solution $\mu_A S = T \cdot \ln(n_A \nu_A)$, while Equation 3.4 states that the chemical potential of the complex is equal to the sum of chemical potentials of A-molecule and j solvent molecules involved in the complex formation $\mu_{SS} = T \cdot \ln(n_S \nu_S)$. Solving equations 3.3 and 3.4 with respect to n_A and n_C gives

$$n_A = \frac{1}{\nu_A} \exp\left(\frac{1}{T}(-\epsilon + \gamma \cdot \frac{2}{R})\right) \tag{3.5}$$

$$n_C = \frac{1}{\nu_C}(n_S \nu_S)^j \exp\left(\frac{1}{T}(-\epsilon_C - \epsilon + \gamma \cdot \frac{2}{R})\right) \tag{3.6}$$

It is possible to understand qualitatively the temperature effect on n_P by considering the particle size to be large enough, far from its critical value. In this case the surface energy contributions in the exponents of Equations 3.5 and 3.6 can be neglected, taking the limit $\gamma \to 0$. In this limit the number fraction of precipitated A-molecules is

$$n_P \nu_A \approx m_A \nu_A - \frac{\nu_A}{\nu_C}(n_S \nu_S)^j \exp\left(\frac{\epsilon_C - \epsilon}{T}\right) - \exp\left(-\frac{\epsilon}{T}\right) \tag{3.7}$$

Taking the derivative with respect to temperature we obtain

$$\nu_A \frac{dn_P}{dT} = \frac{1}{T^2} \cdot \exp\left(-\frac{\epsilon}{T}\right) \cdot \left(-\epsilon + \frac{\nu_A}{\nu_C} \cdot (n_S \nu_S)^j \cdot (\epsilon_C - \epsilon) \cdot \exp\left(-\frac{\epsilon_C}{T}\right)\right) \tag{3.8}$$

For $\frac{dn_P}{dT} < 0$ the precipitate mass, namely the A-particle size, would decrease with increasing temperature, as observed for most materials precipitating from solution. On

the other hand, for $\frac{dn_P}{dT} > 0$ an increase in temperature would result in an increase in the precipitate number of A-molecules, as experimentally observed for hybrid perovskites. From Equation 3.8 we can see that this phenomenon takes place if

$$\epsilon_C > \epsilon \cdot \left(1 + \frac{\nu_C}{\nu_A} \cdot (n_S \nu_S)^{-j} \cdot \exp\left(-\frac{\epsilon_C}{T}\right)\right) \tag{3.9}$$

or equivalently that

$$\frac{\nu_C}{\nu_A} \cdot (n_S \nu_S)^{-j} \cdot \exp\left(-\frac{\epsilon_C}{T}\right) \ll 1 \tag{3.10}$$

that means large enough ϵ_C/T ratio, so that we obtain $\epsilon_C > \epsilon$. This can be further understood in the following terms. At low temperatures most of the A-molecules are bound with solvent in the complexes, so the solution has no supersaturation in terms of concentration of unbound A-molecules. When temperature increases the concentration of unbound A-molecules increases because of the dissociation of the complexes, eventually reaching the supersaturation and triggering the precipitation of A-particles. Viceversa, when the temperature of the solution is decreased, the concentration n_A of unbound A-molecules is also decreased because of formation of more complexes with solvent. This decrease in n_A concentration makes the solution too diluted in A-molecules so that the particle has to transfer some molecule to the solution, dissolving.

3.1.2 Seed assisted ITC

ITC is a widely used simple low temperature growth method, employed to grow hybrid perovskites single crystals in hours rather than days. However, a systematic study of this technique promoted by Amari *et al.* [31] revealed poor reproducibility and poor controlling of crystal quality, leading to the growth in large proportion of polycrystals and high strained single crystals. They propose a complementary method for ITC crystal growing employing MAPbBr$_3$ crystal seeds in order to increase significantly the reproducibility of the process and the quality of as-grown crystals.

Using the unseeded growth protocol (standard ITC) lead to the formation of crystals where maximum dimensions are limited by the volume of the used solution (4.5 mm× 4.5mm × 1.5 mm obtained in 1mL of solvent), with an average number of 2 crystals formed in each vial. The crystals spontaneously nucleated at the air-solution meniscus before falling at the bottom of the vial. As aforementioned, the outcome of this technique is divided in polycrystals and single crystals. These latter were studied with polarized light microscopy and chemically etched, showing high dislocations density (Figure 3.2).
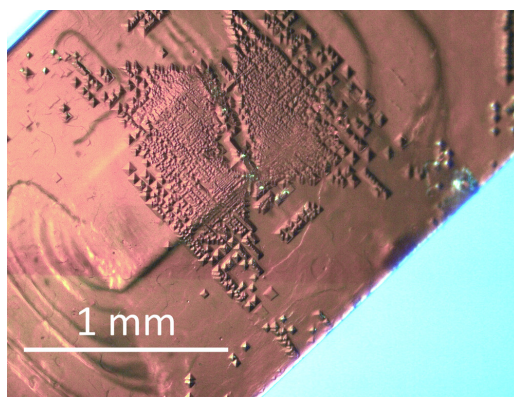
Figure 3.2: *Optical image of chemical etched best crystal growth with the standard ITC protocol. The high density of dislocations surrounding the nucleation site is clearly visible. [31]*

From this analysis Amari *et al.* illustrated that one of the main causes of lack of reproducibility of the ITC standard method is the uncontrolled quality of spontaneous nucleated seeds. Even when a single crystal is formed, the seed strongly impacts on the final structural defect density because strains and dislocations can propagate in the growing crystal.

From these considerations the same authors implemented the seed assisted ITC growth method. In this technique MAPbBr$_3$ crystal seeds were prepared following the standard ITC method and well selected. The chosen seed was then moved into a new vial with MAPbBr$_3$ molar solution thermalized at $\approx 50°$, inserted in an oil bath keeping the solution meniscus slightly above the oil level in order to avoid any spurious spontaneous nucleation. In order to take full advantage of seeded growth using seeds with minimum strains, the temperature increase should be slow enough to allow unstrained seeds to grow significantly and hence desaturate the solution to avoid reaching too high supersaturations. This condition was achieved with a linear temperature profile with an increase rate of 5°C/h. Following this protocol, they obtained high quality single crystals. This is because under these conditions, growth rates are driven by the supersaturation limited by the temperature linear profile, so that the growth kinetics becomes seed quality independent. Moreover, as the supersaturation is limited during all the growth process, no growth instability occurs.
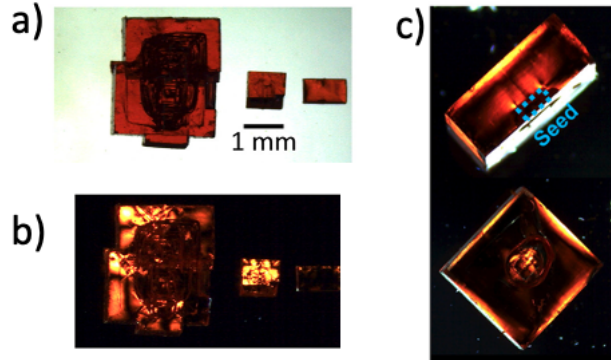
37

Figure 3.3: *(a) Photograph of typical crystals obtained for the unseeded step protocol, from left to right polycrystal, single crystal with strains, single crystal free of strain; (b) Same crystals observed between crossed polarizers; c) Best single crystals grown using the linear temperature profile observed between crossed polarizers (side and top views) [31].*

MAPbBr$_3$ single crystals characterized in this work were fabricated using the seed assisted ITC. CH$_3$NH$_3$Br ($\geq$ 99%, anhydrous), PbBr$_2$($\geq$ 98%) and DMF($\geq$ 99.8%, anhydrous) were purchased from Sigma-Aldrich and were used without any purification. We prepared a 1M 5mL solution in 20 mL vial, stirring the two precursors with DMF overnight, then filtered it with PTFE 0.2 μm filter. Seeds were grown following the standard ITC technique, heating up the solution to 85°C in the oil bath, wait for spontaneous nucleation and choosing only the best crystal seeds. For crystal fabrication we prepared a solution identical to the one for seeds growth and heat it up to 55°. Once the temperature was reached, we choose two seeds and placed them in the heated solution, paying attention to keep them far from the vial walls, but positioning them far enough from each other to avoid merging. Then, we heated up again the system to 60° from which we started the linear temperature ramp to 85°C with temperature rate of 5°C/h. We obtained two $MAPbBr_3$ cubic crystals with average dimensions of 5mm×5mm×2mm.

Finally, we performed a chemical etching of the crystal surface. This was performed employing six solutions of DMF with different concentrations of chlorobenzene (CB), from 75% to 100%. The crystals were moved from the growth solution to the etching solution with the lowest CB concentration. Then, the crystal was moved to the following solutions, with increasing CB concentration. DMF present in the first vials melts the small nanocrystals that deteriorate the surface quality.

The samples measured in this work consist of MAPbBr$_3$ crystals sandwiched between two ohmic contact or connected with co-planar contacts (Figure 3.4a and b, respectively). In both cases, 30 nm chromium contacts were thermally evaporated on the crystal. Figure

3.4 illustrates how the chromium contacts are connected to copper pads using copper wires and silver paste. Such a system is mounted on a thermoconductive, but electrically insulating mica substrate.
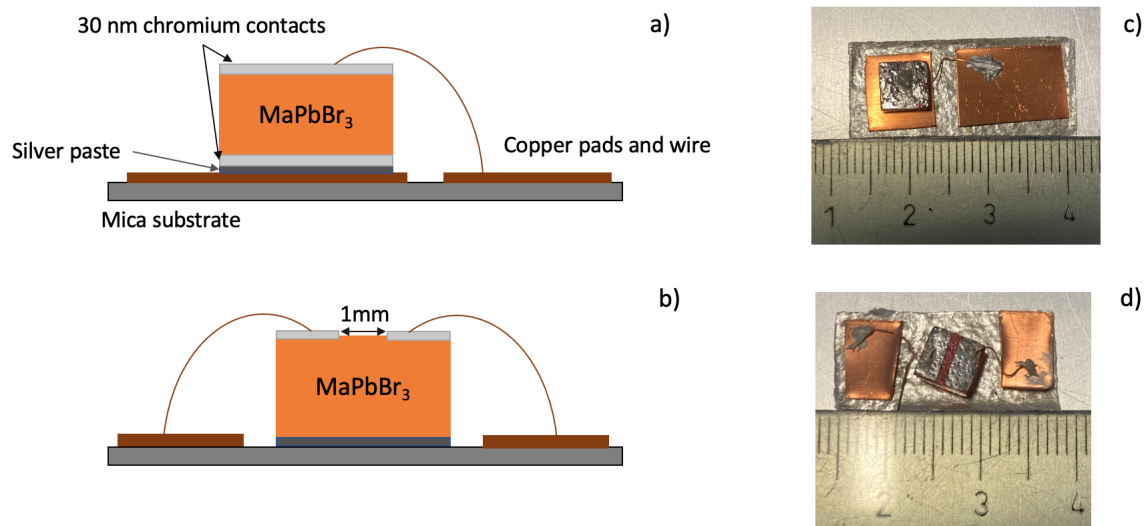

Figure 3.4: *On the left: Scheme of $MAPbBr_3$ crystal with chromium ohmic contacts mounted on mica substrate: a) stacked geometry; b) co-planar geometry. On the right: photograph of measured samples with c) stacked and d) co-planar geometry.*

3.2 PICTS

3.2.1 Experimental set-up

As mentioned in Chapter 1, defect characterization is one of the remaining issues to develop state of art perovskites-based devices. In this thesis we characterize defects in MAPbBr$_3$ single crystals, fabricated as described in the previous section, with Photo Induced Current Transient Spectroscopy (PICTS). In Chapter 2 we described the physical principles on which this technique is based, while this chapter will present the experimental set-up used to carry out the measurements. In order to acquire a PICTS signal, a photocurrent induced by the illumination of the sample is measured using the following experimental set-up.
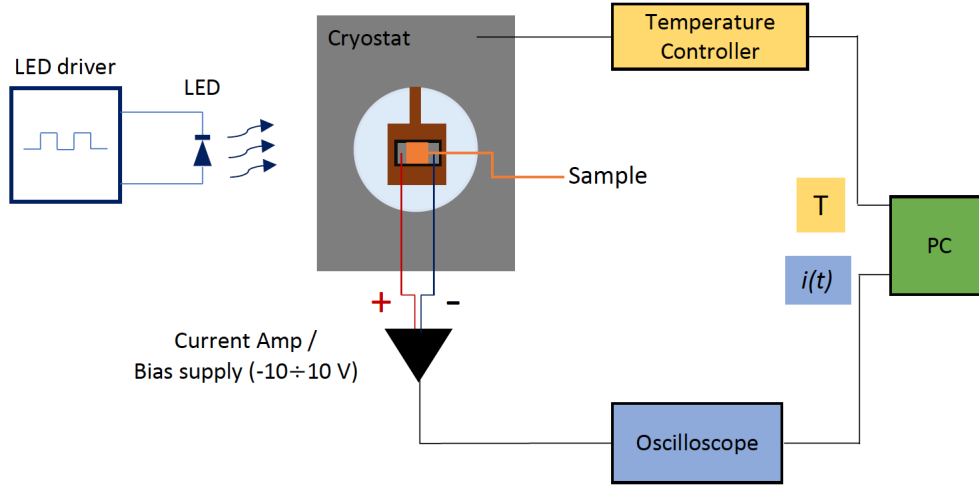
Figure 3.5: *Experimental set up used for PICTS: the illumination source is a led modulated by a square wave; the sample is placed in a cryostat under vacuum; Temperature is regulated by a PID temperature controller during the temperature scan; both temperature and photocurrent signal are acquired by a DAQ acquisition board connected to a computer.*

The scheme of the set-up employed to carry on the measurement is presented in Figure 3.5. The illumination source is a LED modulated by a rectangular wave, placed in the front of the cryostat chamber transparent window. The sample, composed as described in the previous section, is mounted on the cold finger and inserted in the cryostat in such a way that the sample is aligned with the LED. Once closed, the chamber is pumped down to 10^{-4} mbar with a rotary pump. The temperature is controlled by two sensors, a diode, placed on the cryostat cold finger, monitoring the sample temperature and a thermocouple regulating the PID feedback control. The signal is collected with a BNC cable, amplified by a current amplifier, which also provides a bias supply to the sample and collected by a data acquisition board (DAQ). This latter is driven by a LAbView software installed on the laboratory computer.

3.2.2   Data analysis

The basis of the data analysis in PICTS is the rate window method. This method can be developed in many variants as described by Balland *et al.* [32]. In general, it consists of sampling the photocurrent signal in either two or four points along the photocurrent decay. In the former case, the analysis technique is called "double-gate PICTS", in the latter "four-gate PICTS". Such set of gates (either two or four) represents a rate window.
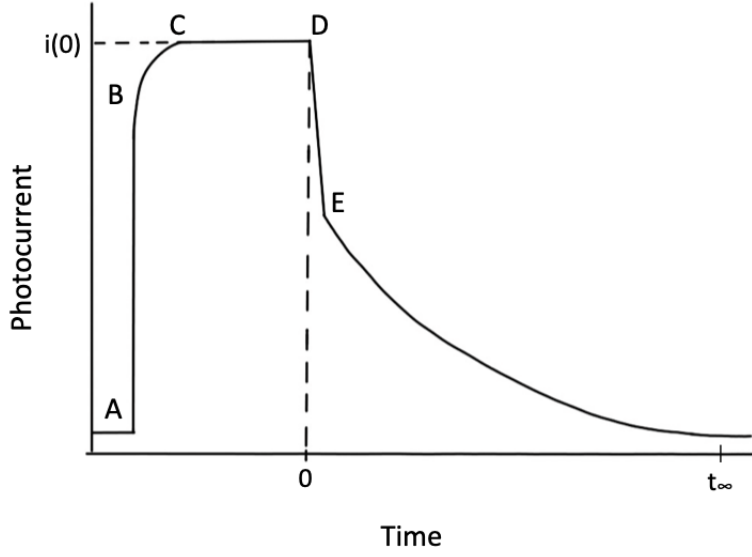
Figure 3.6: *Transient photocurrent response to a pulsed light turned off at t=0.* t_∞ *corresponds to the dark current.*

Figure 3.6 shows an example of transient photocurrent measured in response to a light pulse. In the region from A to B photo-carriers produced by light are excited to the corresponding bands. Between B and C trapping occurs until a quasi-stationary state is reached. At t=0 the light is turned off, and the current drop from D to E corresponds to recombination. The current exponential decay induced by detrapping in the range EF is the component of interest of PICTS measurements and is defined as described in Equation 2.40

$$i(t) = -eE\tau_n\mu_n e_n n_t(0)\exp(-e_n t)$$

where $-e$ is the electronic charge, $\vec{E}$ is the applied electric field to the sample, μ_n is the electron mobility, τ_n is the recombination lifetime, $n_t(0)$ is the initial density of filled traps. The emission rate depends on the trap activation energy E_a and trap cross section σ_{na} as described by Equation 2.28

$$e_n = \gamma T^2 \sigma_{na} \exp\left(-\frac{E_{na}}{kT}\right)$$

Double-gate method

Considering the product $\mu_n\ \tau_n$ and $n_t(0)$ in Equation 2.40 temperature independent, the double gate method consists in plotting the current difference
$\Delta_{12}i(T) = i(t_1) - i(t_2)$ measured at the two gate times (t_1 and t_2), resulting in a spectrum

41

consisting of current signal as a function of temperature. Such signal is recorded for several sets of rate windows, provided that t2/t1 is held constant. This results in a series of PICTS spectra, one for each rate window. An example of PICTS spectra is shown in Figure 3.7(right). A crucial point when using the double gate method is to make sure that the initial trap filling n_t remains constant over the scanning temperature range. This is fulfilled using high photo-excitation in order to saturate the traps. In this condition the peak maximum is defined for

$$e_n = \frac{1}{t_1 - t_2} \ln\left(\frac{1 - e_n t_2}{1 - e_n t_1}\right) \tag{3.11}$$

Being a transcendental equation, 3.11 must be solved numerically via software analysis.
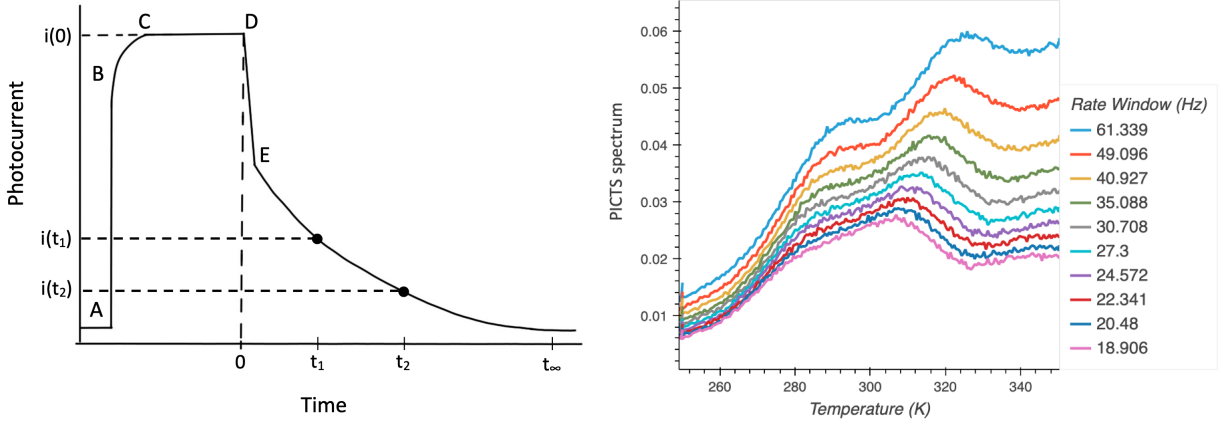

Figure 3.7: *On the left: Transient photocurrent response to a pulsed light turned off at t=0 where t_1 and t_2 are the two gate times at which the current is sampled; On the right: typical PICTS spectra where different colors show different rate windows.*

Experimentally we perform a gaussian fit of the peaks, extrapolating the temperature T_m at which the maximum of the peak occurs. Following Equation 2.28 we obtain

$$\ln\left(T_m^2/e_n\right) = \gamma\sigma + \frac{E_a}{K_B T_m} \tag{3.12}$$

hence plotting $\ln(T^2/e_n)$ as a function of the inverse of the temperature (usually 1000/T), we obtain an Arrhenius plot as in Figure 3.8 (right). In this way we extrapolate the trap activation energy and capture cross section from the slope and the intercept of the curve, respectively. In addition, if the $\mu\tau$ product is known, the double-gate processing allows us to obtain the value of $n_t(0)$ and hence the trap concentration.
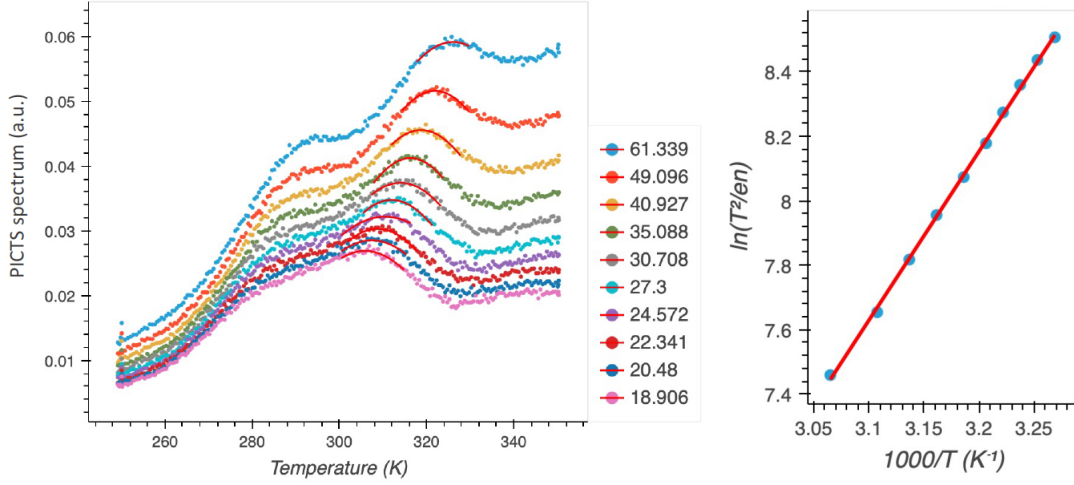
42

Figure 3.8: *On the left: example of gaussian fit performed on the spectrum peaks; On the right: example of Arrhenius plot extrapolated from the fitting of the curves.*

Lifetime and mobility of the thermally released carriers could depend on temperature, introducing artifacts in the measurement. Indeed, in this case any change in $\Delta i(T)$ could be due not only to a change in the decay process (exponential part of Equation 2.40), but also to a change in the relative signal height (pre-exponential part in Equation 2.40). This problem is solved by normalising $\Delta_{12}i(T)$ by the photocurrent $\Delta i_L(T) = i(0) - i(t_\infty)$. However, it is important to highlight that normalising the signal does not allow for the evaluation of the trap concentration.

A variation to this method, used to enhance the signal to noise ratio of PICTS analysis, was employed by Pecunia *et al.* [33]. The difference from the "standard-double gate" method is that PICTS signal is evaluated considering the integral of the current with respect to the selected rate window, rather than its difference. In this way the signal is defined as

$$S_i(T; t_1, t_2) = \int_{t_1}^{t_2} i(T; t) dt \tag{3.13}$$

Four-gate method

The double-gate method described above depends on some assumptions that in general could not be fulfilled. The first hypothesis assumes the product $\mu_n \tau_n$ and $n_t(0)$ to be temperature independent. In general it is not easy to take into account possible thermal variations of mobility and recombination lifetime. Additionally, it is not possible to know a priori that $n_t(0)$ remains constant over the whole temperature range. Finally there is some uncertainty due to the presence of the e_n in the pre-exponential factor,

43

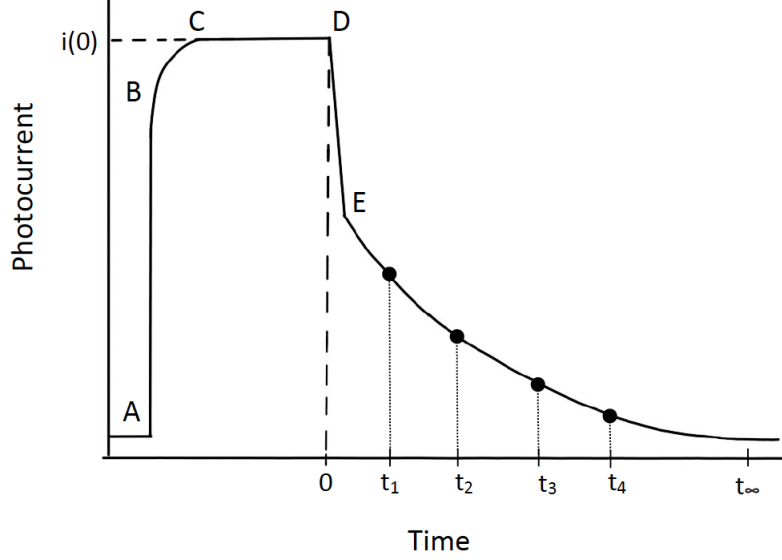leading to some problems in the evaluation of Equation 3.11.

Figure 3.9: *Current transient induced by a pulsed light where time points for the four-gate method signal processing are highlighted.*

These arguments led Balland *et al.* to introduce the four-gate signal processing. It consists in sampling the current signal at four delay times t_1, t_2, t_3 and t_4 as shown in Figure 3.9 and computing the ratio

$$S_{4g} = \frac{i(t_2) - i(t_3)}{i(t_1) - i(t_4)} \tag{3.14}$$

Using Equation 2.40 this takes the form

$$S_{4g} = \frac{\exp(-e_n t_2) - \exp(-e_n t_3)}{\exp(-e_n t_1) - \exp(-e_n t_4)} \tag{3.15}$$

This equation goes through a maximum if t_1 and t_4 lie outside the range t_2-t_3. The peak maximum is simply related to the delay times only if the second term of the denominator of Equation 3.15 is negligible, namely for $t_4 \gg t_1$. When this condition is satisfied the peak maximum occurs for the rate window value:

$$e_n = \frac{1}{t_3 - t_2} \ln\left[\frac{t_3 - t_1}{t_2 - t_1}\right] \tag{3.16}$$

Also in the case of the four-gate processing method an integral variant was implemented. In this case the signal is defined as

44

$$S_{4g}(T; t_1, t_2) = \frac{\int_{t_2}^{t_3} i(T; t)dt}{\int_{t_1}^{t_4} i(T; t)dt} \qquad (3.17)$$

leading to the same expression as Equation 3.16 for the peak maximum.

We note that both the normalised signal processed with the standard double gate method and the one obtained from the four-gate method do not allow for the evaluation of the concentrations of trapping levels due to the normalization procedure that deletes any information on the pre-exponential factor of Equation 2.40.

3-dimensional visualization of PICTS spectra

The spectra visualization depends strongly on the rate windows choice during the analysis. In this case a large number of rate windows are generated in order to span over the hole transient, producing the corresponding PICTS spectra. These are then plotted in a three dimensional map as shown in Figure 3.10. This enables a more easy and immediate trap visualization.
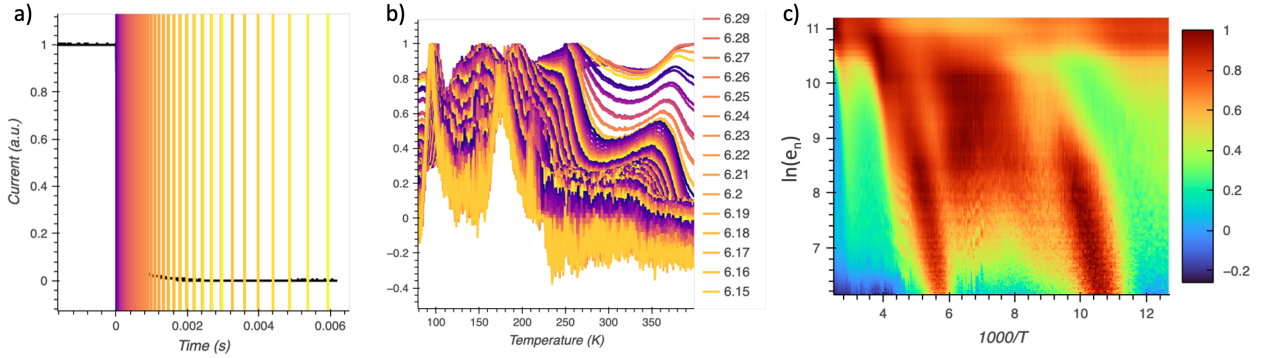

Figure 3.10: *a) Generation of a large number of rate windows spanning over the whole transient; b) corresponding PICTS spectra; c) three dimensional map.*

Chapter 4

Results and Discussion

4.1 Test of data analysis methods on a stable known semiconductor (CdTe)

In Section 3.2.2 we described the four different data processing techniques available for PICTS analysis: double-gate and four-gate, both in standard and integral version. In order to check the reliability of these methods, we performed two subsequent scans on a known sample of cadmium telluride (CdTe), a stable crystalline semiconductor. The data acquired from both scans were analysed following the four methods, obtaining four different spectra. Figure 4.1 highlights the differences between the four different spectra obtained from the analysis of the first scan data. From a first qualitative analysis of these spectra it is possible to notice that the number of peaks, varies considering different data processing. The spectra evaluated following standard and integral double-gate methods with the same rate windows are showed in Figure 4.2a and b respectively. For sake of clarity in the following analyses, traps extrapolated from the same spectrum will be labeled with integer numbers from 1 to n, starting from left to right.

From this comparison we can notice that the integral method leads to a smoother signal. However, it seems to hide some information as it shows less peaks than the standard method.
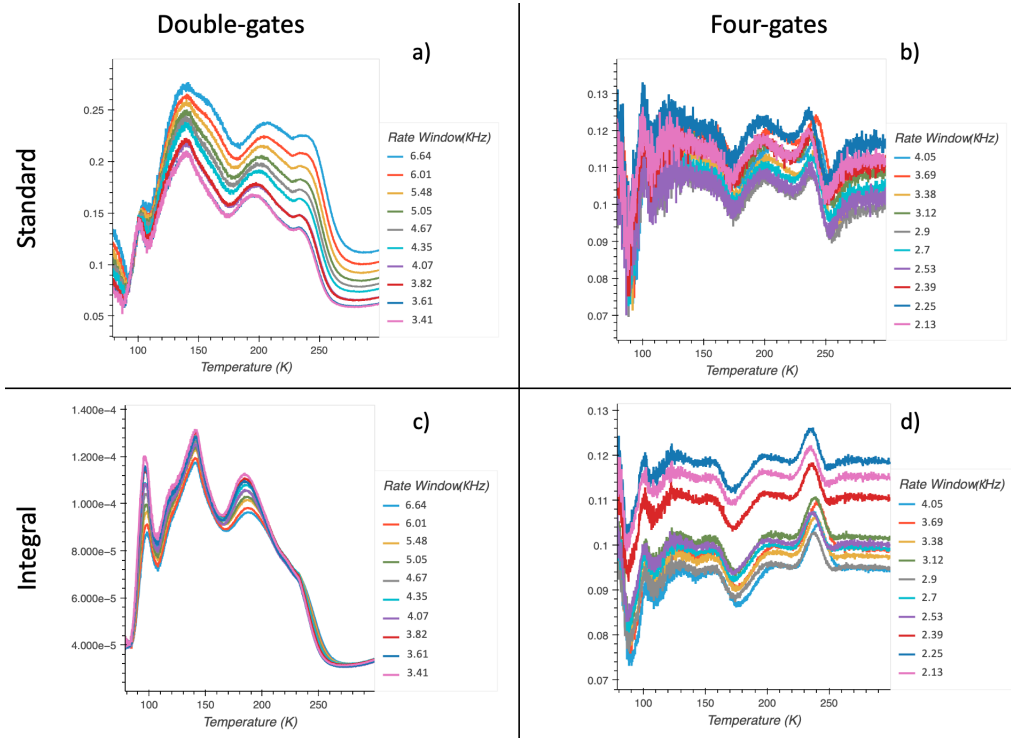
Figure 4.1: *PICTS spectra of CdTe sample obtained analysing the same scan data with standard and integral double-gate and standard and integral four-gates methods.*
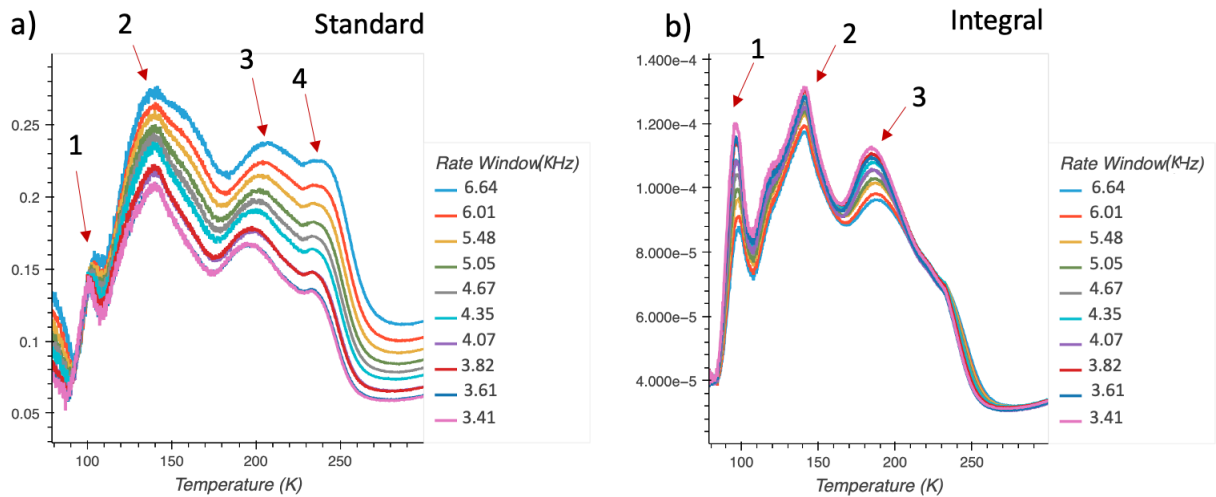

Figure 4.2: *Comparison of PICTS spectra obtained with a)standard and b) integral double-gate methods using the same rate windows.*

Comparing four-gate standard and integral spectra leads to different considerations: in this case the number of peaks remains constant while the signal is less noisy in the integral method with respect to the standard one (Figure 4.3).
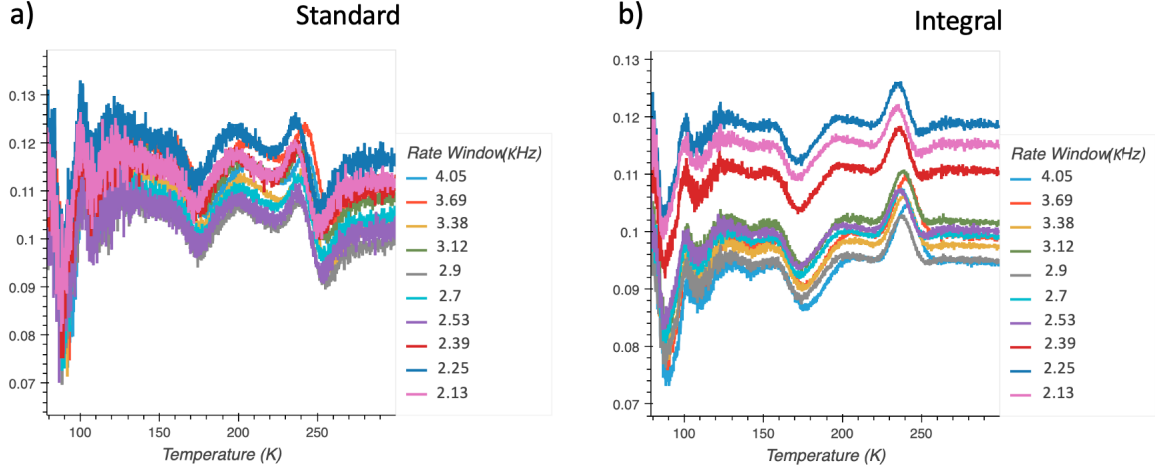

Figure 4.3: *Comparison of PICTS spectra obtained with a)standard and b) integral four-gate methods using the same rate windows.*

Finally, comparing both standard methods (Figure 4.2a and 4.3a), we notice that the four-gates method is more affected by noise with respect to the double-gate processing. Moreover, we can distinguish a variation in the number of peaks between the two spectra, observing that the standard four-gates method resolves peaks not clearly visible in the standard 2 gates method. In Figure 4.2a the second red arrow highlights a predominant peak convoluted with a smaller one on its right. In the four-gates spectrum in Figure 4.3a, in the same temperature range of 120-180 K, we observe two different peaks.

From the analysis of the second scan we obtained again four spectra with the same characteristics.

Consequently, we perform a quantitative analysis of these spectra. We first compare the Arrhenius plots of the traps obtained with the same method in both scans to check for reproducibility of the single methods (Figure 4.4 a-b and Figure 4.5 a-b). As CdTe is a stable inorganic material, we expect to find the same signature Arrhenius plots between different scans.
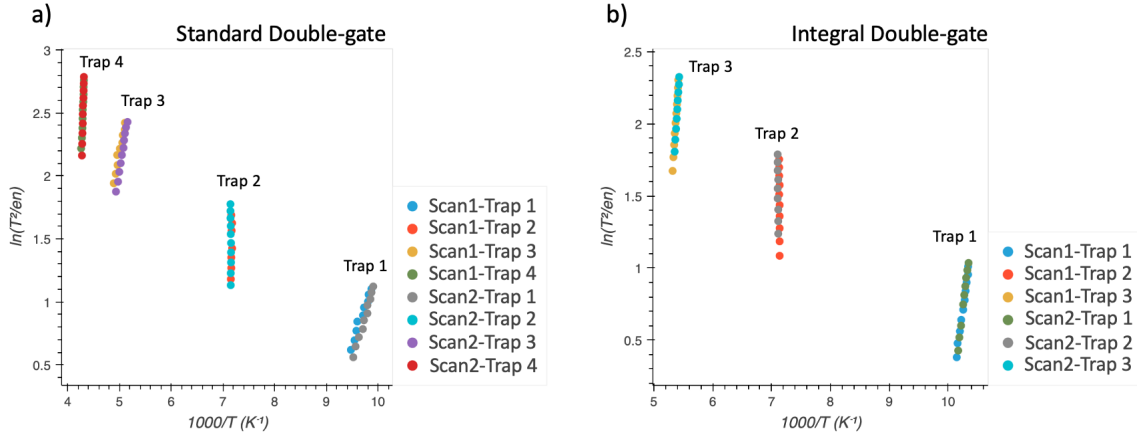
Figure 4.4: *a) Arrhenius plot of traps obtained from the standard double-gate analysis of first and second scan; b)Arrhenius plot of traps obtained from the integral double-gate analysis of first and second scan.*
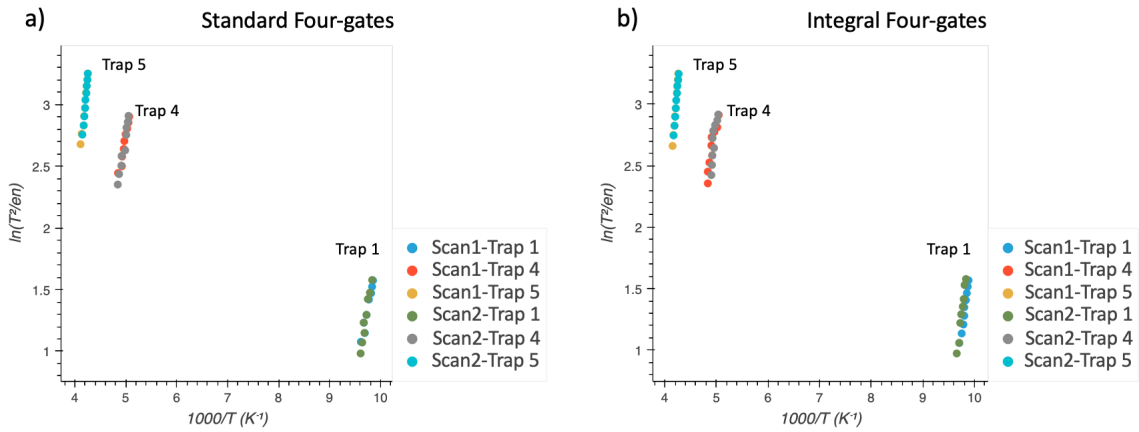

Figure 4.5: *a) Arrhenius plot of traps obtained from the standard four-gate analysis of first and second scan; b)Arrhenius plot of traps obtained from the integral four-gate analysis of first and second scan. In these plots the peaks corresponding to Trap 2 and 3 could not be fitted.*

As predicted, we find the curves corresponding to the same trap extrapolated from both scans to be superimposed one on the other for all the four methods. Moreover, in Figure 4.4b we can notice that the curve corresponding to Trap 2 has a negative slope, meaning a negative activation energy. This unphysical feature could be due to the fact that Trap 2 is not an actual trap, but rather an artifact.

Likewise, we check for the comparability of the methods, comparing the curves of the same trap obtained with the four data processing. To perform this test we choose Trap

1, in the temperature range 90-120 K common to all the spectra. In this case we find that the integral double-gates method is less comparable with the other three methods. Actually, Figure 4.6 shows that the red curve obtained from the integral double-gates method is not aligned to the other three curves.
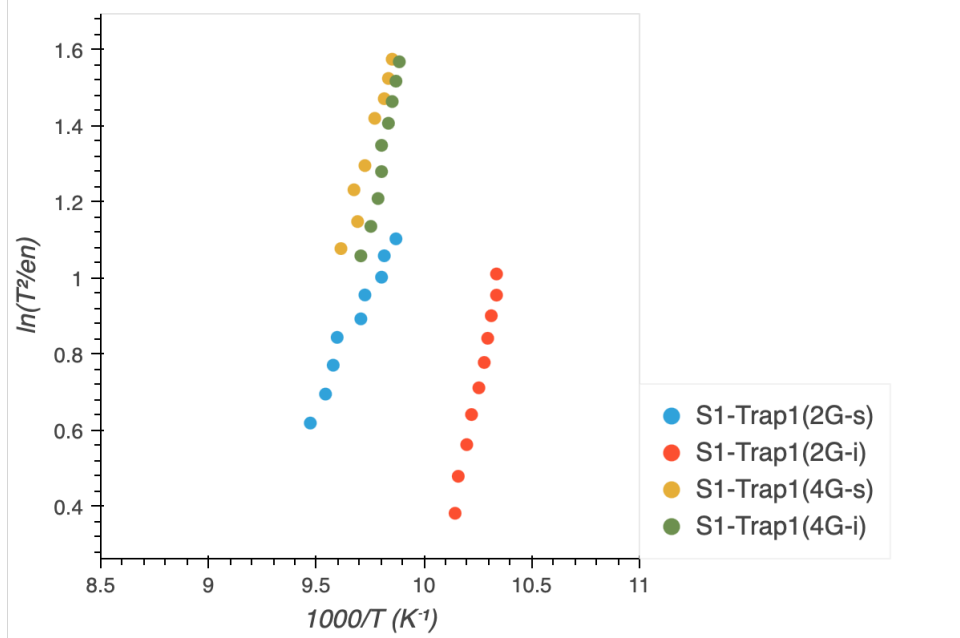

Figure 4.6: *Arrhenius plot of Trap1 curves obtained with the four methods.*

From this analysis we can conclude that the integral double-gate method is the least reliable. Indeed, performing this data analysis on several measurements always led to results that substantially differ from the other three methods outcome. Even if this data processing leads to a smoother spectrum, it shows a lower number of peaks, therefore hiding information, also introducing artifacts. On the other side, the integral four-gates method resolves peaks that are slightly visible in the standard double-gate spectrum, leading to a smoother spectrum with respect to the standard four-gates spectrum. The methods main features are summarized in Figure 4.7.

Regardless of the differences in the data analysis methods, we observe that the PICTS technique is reproducible. Hence, the differences in the Arrhenius plot trap signatures obtained from perovskite samples are due to material related issues as the lack of stability, and not to artifacts induced by the measurement itself.

Type of data analysis method	Data reproducibility	Noise	Comparability with the other methods
Standard double-gate	✓	Low	✓
Integral double-gate	✓	Low	✗
Standard four-gate	✓	High	✓
Integral four-gate	✓	Low	✓

Figure 4.7: *Comparison of the main features of the four different data analysis methods.*

4.2 Electron and hole traps

Once stated the methods reliability, we performed PICTS measurements on a perovskite single crystal sample, electrically connected with top and bottom chromium contacts, as described in Section 3.1.2 in Figure 3.4 (a and c), analyzing the data with standard double-gate processing method.
We performed two scans, biasing the sample with +5V and -5V in subsequent measurements, in order to probe electron and hole traps respectively (as explained in Section 2.2). Other two scans were performed one week later, to check for stability.

Hole traps

Figures 4.8a and 4.8b show the standard PICTS spectra of the positively biased sample obtained from a first measurement and the second one. First, observing the first scan we resolve one evident peak in the standard spectrum, while two peaks are clearly visible in the second one. By fitting them we obtain the Arrhenius plot displayed in Figure 4.9, showing two similar traps between the first and second measurement (yellow and light blue scatter lines). The extrapolated energy values for hole traps are listed in Table 4.1.
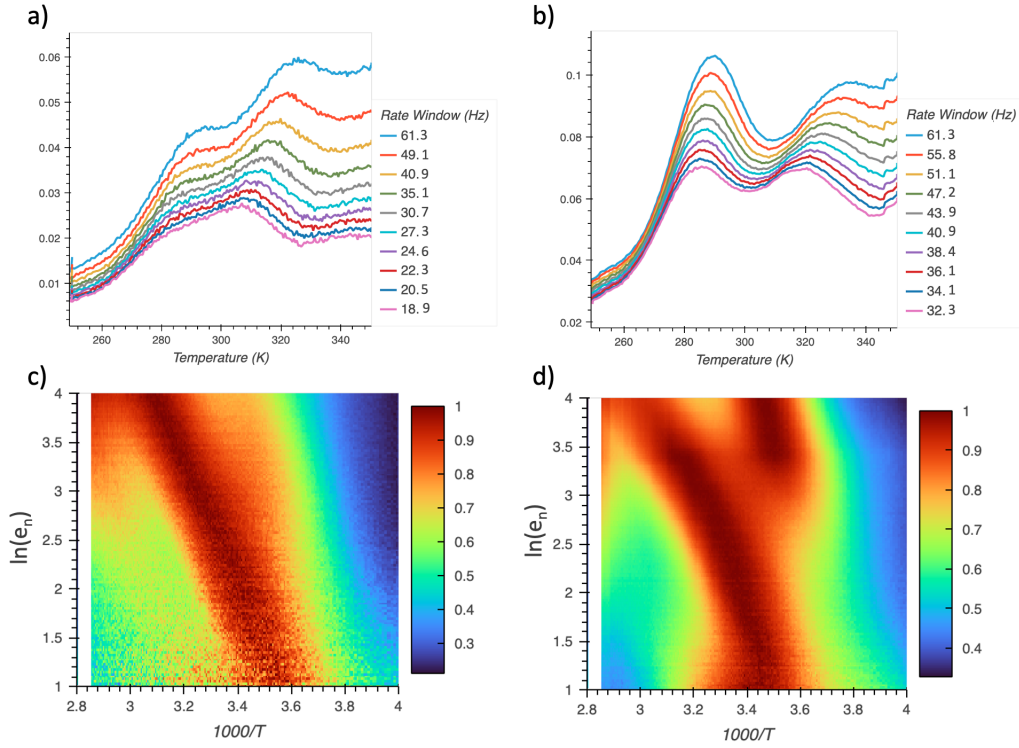
Figure 4.8: *Standard PICTS spectra and PICTS map of first (a and c) and second scans (b and d), obtained positively biasing the sample.*

For better comparison, it is useful to consider the corresponding PICTS maps, reminding that the x axis goes as $1000/T$ and that it permits a better visualization of the spectra thanks to the higher number of rate windows (Figures 4.8c and 4.8d). Here a dark red linear area is clearly visible in both graphs, confirming the Arrhenius plot analysis. Moreover, the relative intensity of the two peaks visible across the colormap plots is changing from the first to the second scan, highlighting in the second scan a second feature that was barely visible in the first one.
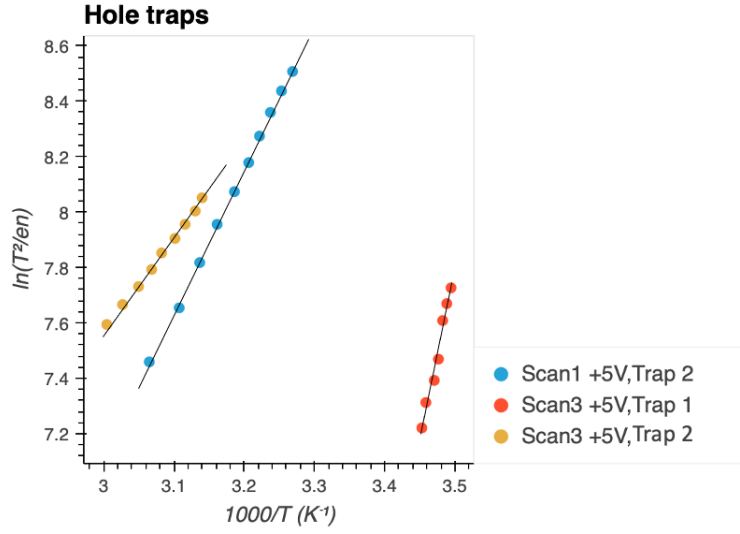
Figure 4.9: *Arrhenius plot showing the trap curves obtained in the first and second scans, where the black solid lines are the linear fit. In the first scan spectrum, the peak related to Trap 1 could not be fitted, hence there is no data to be compared.*

	First scan	Second scan
Trap 1 (eV)	/	1.059± 0.072
Trap 2 (eV)	0.451±0.004	0.287± 0.005

Table 4.1: *Activation energies extrapolated from fitting the Arrhenius plot curves.*

Electron traps

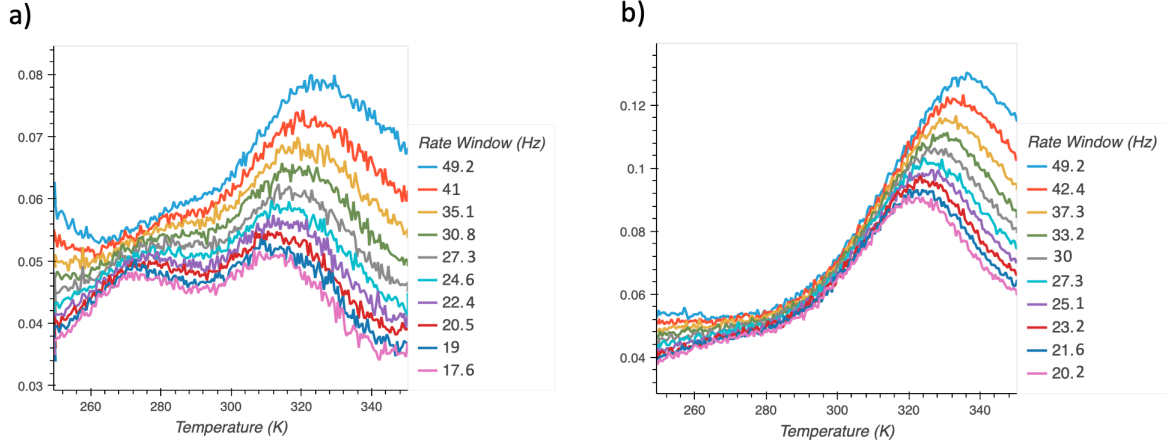The same procedure is followed for the measurements on the negatively biased sample.

Figure 4.10: *Standard PICTS spectra of a) first and b) second scans, obtained by negatively biasing the sample.*

Also in this case a clear peak is evident in both spectra, while the one at lower temperatures is slightly visible in the first scan (Figure 4.10a), disappearing completely in the test measurement (Figure 4.10b). The traps evaluated from fitting these spectra are illustrated in the Arrhenius plot in Figure 4.11, showing good agreement between the trap evaluated from the two measurements. The corresponding values of the activation energies are listed in Table 4.2.
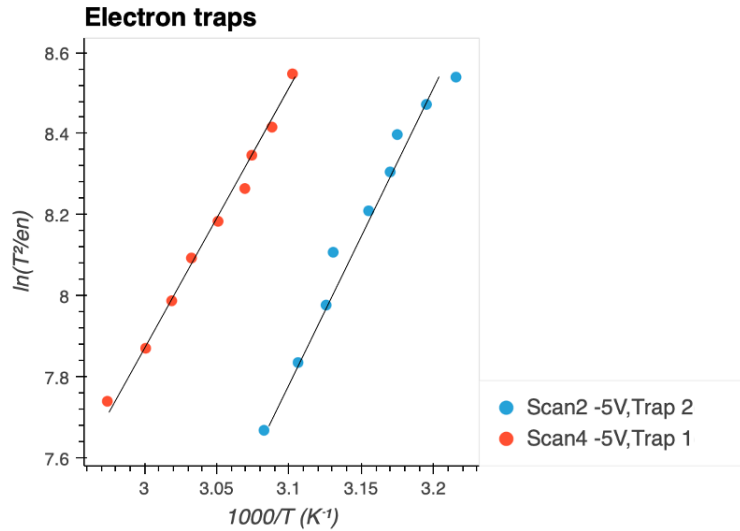

Figure 4.11: *Arrhenius plot showing the trap curves and the linear fit lines, obtained in the first and second scans.*

The comparison of the PICTS maps showed in Figure 4.12 highlights the difference between the two measurements. Besides the evident trap present in both scans, a clearly visible second trap almost disappears in the second scan.
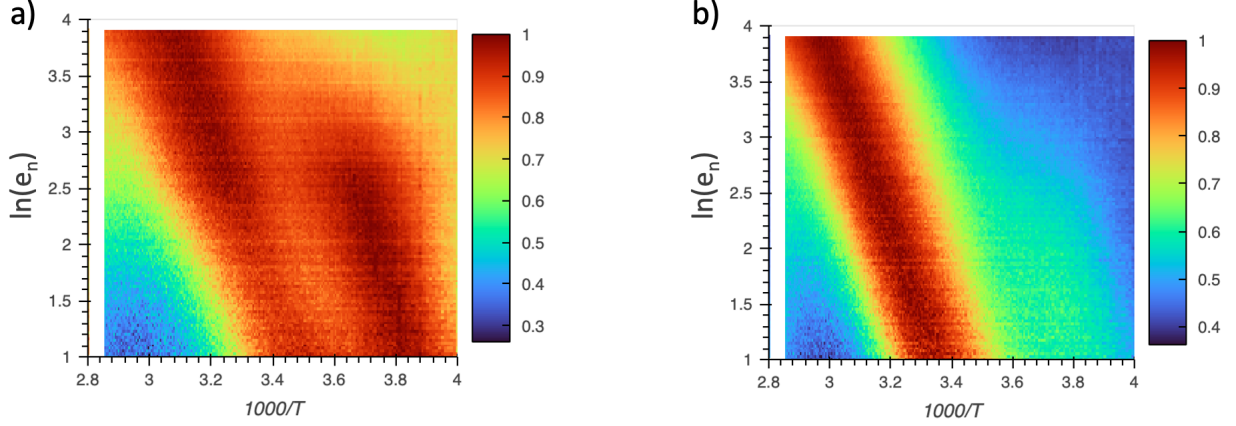

Figure 4.12: *PICTS maps of a) first and b) second scans, obtained positively biasing the sample.*

	First scan	Second scan
Trap 1 (eV)	/	0.533± 0.018
Trap 2 (eV)	0.587±0.036	/

Table 4.2: *Activation energies extrapolated from fitting the Arrhenius plot curves.*

The analysis of this sample points out the unstable nature of hybrid halide perovskites, showing different spectra obtained by measuring the same sample under the same experimental conditions. However, we found an higher reproducibility in activation energy values for negative bias rather than for positive bias.

4.3 Testing bias stress

As seen in Section 4.2, applying opposite sign voltage leads to different traps reproducible in time. Since an applied bias during a small period as the measurement time does not lead to visible effects on traps, we tested the effect of bias in extreme conditions biasing the sample overnight. Actually, MAPbBr$_3$ is employed as active material in ionizing radiation detectors in which the material is subjected to high voltages of the order of hundred of volts.

As demonstrated in Section 4.2, biasing the sample with negative voltage leads to more reproducible traps with similar activation energies. Thus, a first scan was performed, measuring a negatively biased pristine sample in order to have the most favorable conditions for reproducibility. After the measurement, we maintained the negative bias applied

to the sample overnight and then carried out a second scan. Figure 4.13 shows the PICTS spectra corresponding to the pristine sample (Figure 4.13a) and to the overnight biased sample (Figure 4.13b).
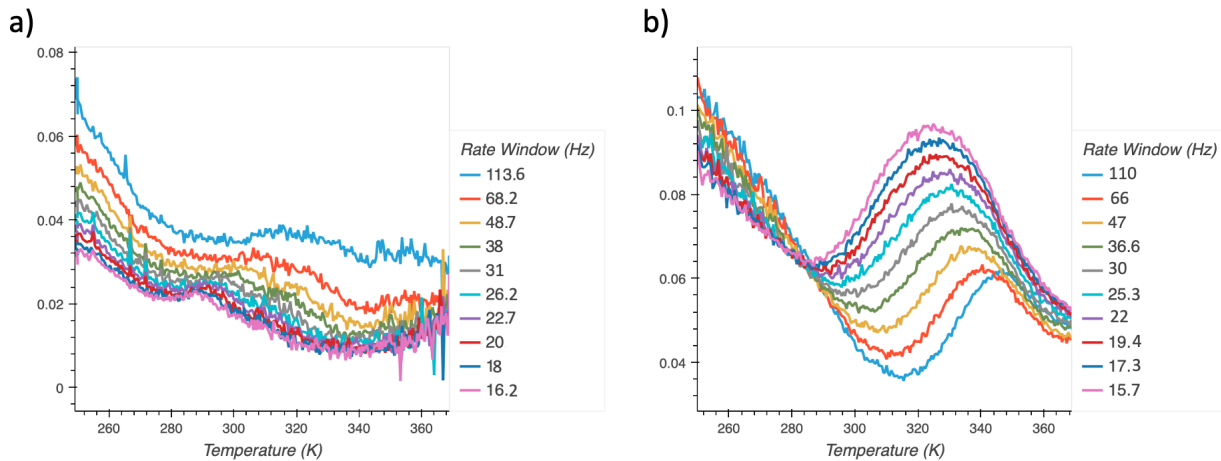

Figure 4.13: *PICTS spectra of a) pristine sample and b) overnight-biased sample.*
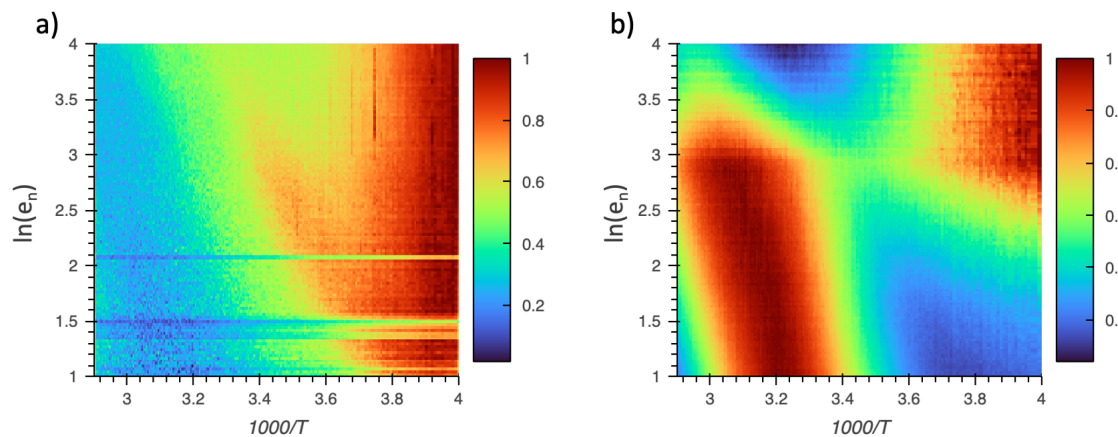

Figure 4.14: *PICTS maps of a) pristine sample and b) overnight biased sample.*

Figure 4.14a shows a dark red vertical area in the low temperature region (right), attributable to an artifact and horizontal lines due to signal noise. However the signature of a traps is visible in the middle of the PICTS map. Conversely, a completely different trap appears in the spectrum of the stressed sample (Figure 4.14b) in the high temperature region. A quantitative comparison between the two traps is shown in Figure 4.15. This Arrhenius plot illustrates two trap signatures of different slopes corresponding to different activation energies, 0.466±0.032 eV and 0.805±0.009 eV, for pristine and bias stressed sample respectively.
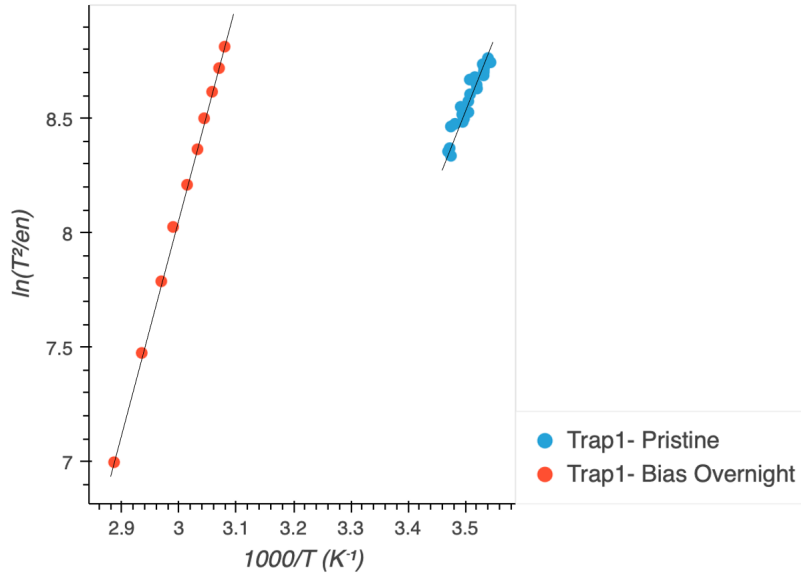
Figure 4.15: *Arrhenius plot of the traps evaluated from fitting the PICTS spectra of Figure 4.13.*

Thus, applying a voltage bias for a long period of time affects the system, leading to different electronic traps. In view of this, it could be interesting to study the bias stress, by varying the time of voltage application and analyzing the material response.

4.4   Checking surface traps contribution

The sandwich contact geometry as described in Figure 3.4a is the standard sample architecture used for PICTS measurements. We tested coplanar contacts geometry as alternative architecture, in order to probe surface traps. To investigate this system we performed two subsequent scans, obtaining the correspondent PICTS maps illustrated in Figure 4.16.
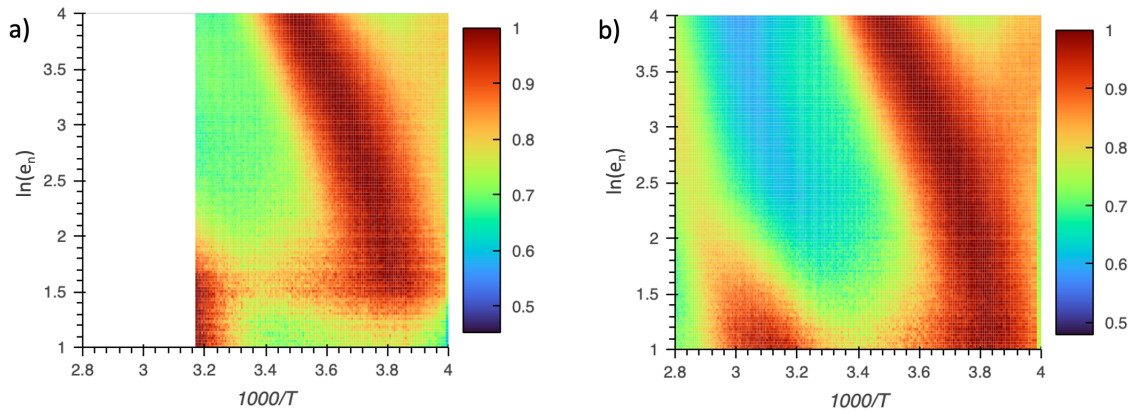
Figure 4.16: *PICTS maps of a) scan one and b) scan two.*

In Figure 4.16a the temperature range is smaller with respect to Figure 4.16b because the abrupt interruption of the first scan at about 315K due to a DAQ system error, hiding some information. Besides this, a clear trap is visible in both PICTS maps, in the high temperature region. Actually, fitting the standard PICTS spectra we obtained the Arrhenius plot in Figure 4.17, showing the reproducibility of Trap 1 in both scans. The activation energy values evaluated from fitting are displayed in Table 4.3.
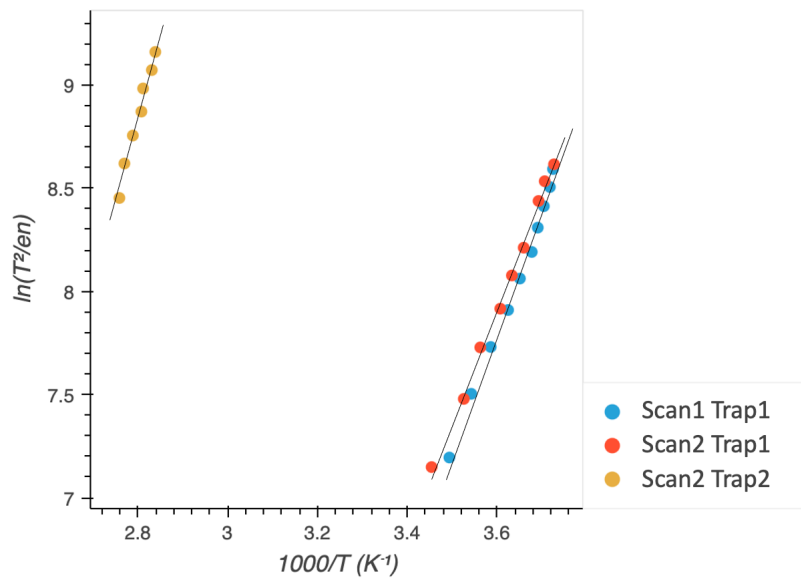

Figure 4.17: *Arrhenius plot showing the traps evaluated from first and second scan*

	First scan	Second scan
Trap 1 (eV)	0.499±0.015	0.473± 0.011
Trap 2 (eV)	/	0.721±0.044

Table 4.3: *Activation energies extrapolated from fitting the Arrhenius plot curves in Figure 4.17.*

Finally, we compare the trap signatures of pristine samples grown in the same solution with different contact geometries in the same Arrhenius plot of Figure 4.18.
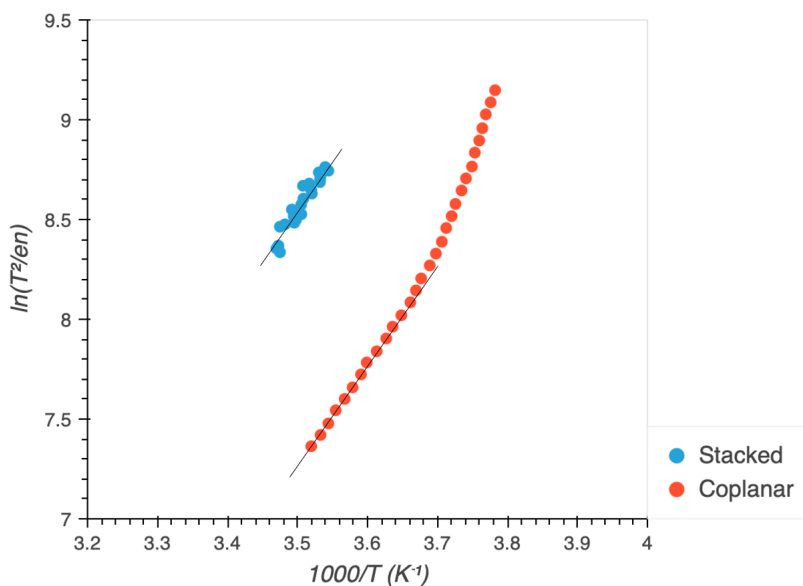

Figure 4.18: *Arrhenius plot of the trap evaluated in stacked and coplanar contacts geometry samples.*

First of all we notice that the trap found in the sample with coplanar contacts (red dots) shows a temperature dependent activation energy, i.e. changing slope with increasing temperature. To compare the two traps we fitted both lines in the same temperature range (270-300K), evaluating similar activation energy values, displayed in Table 4.4, but different capture cross sections. In the sample with coplanar contacts we found a capture cross section one order of magnitude higher than in the standard geometry sample, meaning a trap with the same activation energy of the one in the stacked geometry sample with an higher trapping efficiency.

	Stacked	Coplanar
Activation energy (eV)	0.466±0.032	0.461± 0.004

Table 4.4: *Activation energies measured in two samples with stacked and coplanar contacts geometries.*

Finally, we investigated the effect of using excitation energies lower than the material's band gap. We performed PICTS measurements on the sample employing two different wavelengths, 593 nm and 625 nm. Figure 4.20 shows the photocurrent spectrum of MAPbBr$_3$ in which the arrows highlight the used wavelengths, 474 nm, 593 nm and 625 nm. From this we obtained the two PICTS maps in Figure 4.19, showing a similar trap in all the scans. However, in Figure 4.19b and 4.19c we observe a broader trap signature with respect to the one obtained with standard condition, see Figure 4.19a. Further investigation is needed to account for this broadening.

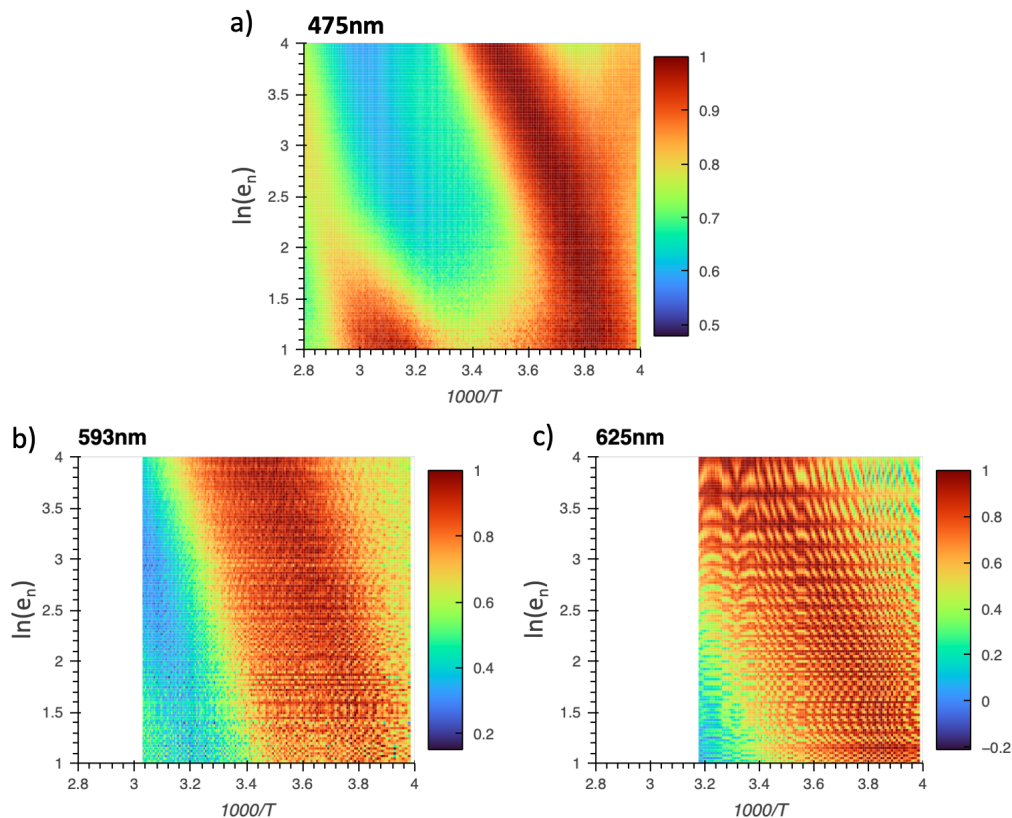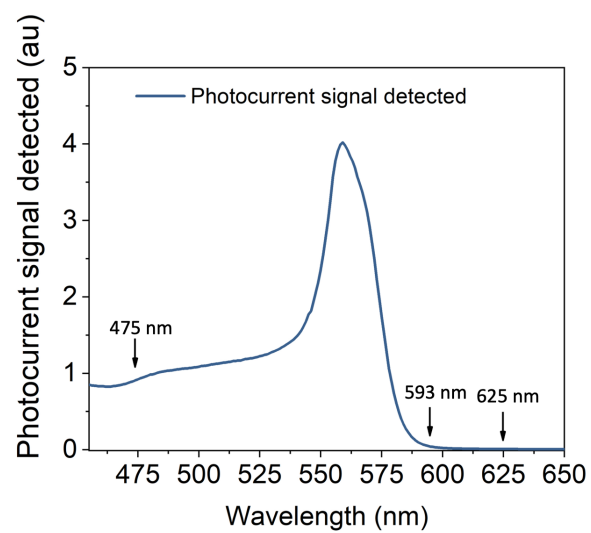Figure 4.19: *PICTS maps evaluated probing the sample with 593 nm and 625 nm LEDs.*

Figure 4.20: *Photocurrent spectrum of a $MAPbBr_3$ single crystal sample with coplanar contacts where the arrows highlight the wavelengths of the LED used in this work.*

Conclusions

Methylammonium lead bromide ($MAPbBr_3$) is an hybrid metal halide perovskite employed in ionizing radiation and LED applications. Understanding the role of defects in the material is crucial for both these technologies. In the first case, defects can act as dopants, increasing the material resistivity leading to higher dark current which is detrimental for radiation detection. On the other hand, defects can serve as non-radiative recombination centers, which is damaging for LED technology.

The main goal of this work is to study $MAPbBr_3$ single crystals defect states, performing Photo-Induced Current Transient Spectroscopy (PICTS), a transient current measurement rarely employed for studying perovskite materials. Since there are four main data processing methods suitable for transient measurements, we first tested the experimental technique and data analysis methods on cadmium telluride (CdTe), a known stable semiconductor.

Once assessed the comparability and reproducibility of the methods, we performed PICTS on $MAPbBr_3$ single crystals. The samples were fabricated following the inverse temperature crystallization technique and then electrically connected with chromium contacts evaporated on top and bottom of the crystal, forming a stacked geometry. This allowed us to probe electron and hole traps independently by changing the sign of the voltage biasing the sample. Thus PICTS measurement on the same sample with negative and positive biases led to different activation energy values, highlighting a better reproducibility when looking for electron traps.

In the following, in order to test the effect of prolonged biasing, usual during radiation detector operation, we tested the bias effect in extreme conditions biasing the sample overnight. To do so, we probed electron traps before and after 12h bias conditioning. We observed a strong change in PICTS maps, presenting two trap signatures different activation energies, 0.466±0.032 eV and 0.805±0.009 eV for pristine and bias stressed sample respectively. Further investigations should be done on this increase in activation energy since usual working conditions of ionizing radiation detectors comprise several hours of bias stress, eventually at higher voltages.

We tested coplanar contacts geometry as alternative architecture, in order to probe surface traps. These measurements showed one highly reproducible trap between scans

with energy values 0.499±0.015 eV and 0.473± 0.011 eV, in the first and second scan respectively. Then, we compared the trap signatures of pristine samples with the two different contact geometries. Fitting both traps in the same temperature range, we obtained two comparable energies 0.466±0.032 eV and 0.461± 0.004 eV in stacked and coplanar geometry samples respectively, but with different capture cross section. The surface trap showed a capture cross section one order of magnitude higher than the bulk trap, meaning an higher trapping efficiency.

Finally, probing the system with a light source of energy lower than the MAPbBr$_3$ energy gap (2.3 eV, 539 nm) we observed a measurable photocurrent. Thus, performing PICTS using three different light sources at 475 nm, 593 nm and 625 nm we measured three spectra showing a similar trap in every scan, showing a broader trap signature with respect to the one obtained with energy higher than the energy gap.

It is interesting to notice that, besides different measurement conditions, trap activation energy values around 0.46 eV are recurrent. In the following plot we summarized the obtained activation energies with respect to the applied bias. We notice that the values obtained at positive biases are more scattered with respect to the ones obtained for negative voltages.
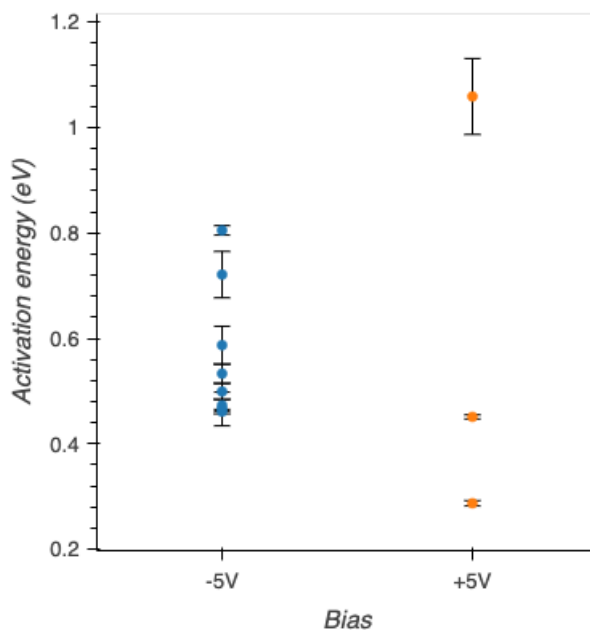

Figure 4.21: *Activation energy values obtained in this work plotted as a function of the applied bias.*

The findings of this work show the presence of a trap level located at 0.46 eV from the band edge. The reproducibility of this result, obtained under different experimental conditions in pristine MAPbBr$_3$ single crystals, suggests that this trap could be related

to point defects related to ion migration phenomena.

Thus, this work could be seen as an important starting point for the investigation of defect states in MAPbBr$_3$ with Photo-Induced Current Transient Spectroscopy. Further investigations will be necessary to account for the nature of different traps and the behavior of the material under different working condition as constant bias applied and aging.

Bibliography

[1] Joshua Maggiora, Feng Li, and Rongkun Zheng. Charge Transport Properties of Methylammonium Lead Trihalide Hybrid Perovskite Bulk Single Crystals. *physica status solidi (RRL)–Rapid Research Letters*, 15(1):2000410, 2021.

[2] Cheng Chen, Xiangmin Hu, Wengao Lu, Shuai Chang, Lijie Shi, Liang Li, Haizheng Zhong, and Jun-Bo Han. Elucidating the phase transitions and temperature-dependent photoluminescence of mapbbr3 single crystal. *Journal of Physics D: Applied Physics*, 51(4):045105, 2018.

[3] Masoumeh Keshavarz, Martin Ottesen, Steffen Wiedmann, Michael Wharmby, Robert KÃ¼chler, Haifeng Yuan, Elke Debroye, Julian A. Steele, Johan Martens, Nigel E. Hussey, Martin Bremholm, Maarten B. J. Roeffaers, and Johan Hofkens. Tracking structural phase transitions in lead-halide perovskites by means of thermal expansion. *Advanced Materials*, 31(24):1900521, 2019.

[4] Noriko Onoda-Yamamuro, Takasuke Matsuo, and Hiroshi Suga. Calorimetric and ir spectroscopic studies of phase transitions in methylammonium trihalogenoplumbates (ii). *Journal of Physics and Chemistry of Solids*, 51(12):1383–1395, 1990.

[5] Hiroyuki Fujiwara. *Hybrid perovskite solar cells : characteristics and operation.* Wiley-VCH, Weinheim, Germany, 2022.

[6] Gregor Kieslich, Shijing Sun, and Anthony K Cheetham. Solid-state principles applied to organic–inorganic perovskites: new tricks for an old dog. *Chemical Science*, 5(12):4712–4715, 2014.

[7] Bethan Charles, Jessica Dillon, Oliver J Weber, M Saiful Islam, and Mark T Weller. Understanding the stability of mixed a-cation lead iodide perovskites. *Journal of Materials Chemistry A*, 5(43):22495–22499, 2017.

[8] Qingdong Ou, Xiaozhi Bao, Yinan Zhang, Huaiyu Shao, Guichuan Xing, Xiangping Li, Liyang Shao, and Qiaoliang Bao. Band structure engineering in metal halide perovskite nanostructures for optoelectronic applications. *Nano Materials Science*, 1(4):268–287, 2019.

[9] Jenya Tilchin, Dmitry N Dirin, Georgy I Maikov, Aldona Sashchiuk, Maksym V Kovalenko, and Efrat Lifshitz. Hydrogen-like wannier–mott excitons in single crystal of methylammonium lead bromide perovskite. *ACS nano*, 10(6):6363–6371, 2016.

[10] Oriane Baussens, Loli Maturana, Smaïl Amari, Julien Zaccaro, Jean-Marie Verilhac, Lionel Hirsch, and Eric Gros-Daillon. An insight into the charge carriers transport properties and electric field distribution of ch3nh3pbbr3 thick single crystals. *Applied Physics Letters*, 117(4):041904, 2020.

[11] Christie LC Ellis, Emily Smith, Hamza Javaid, Gabrielle Berns, and Dhandapani Venkataraman. Ion migration in hybrid perovskites: Evolving understanding of a dynamic phenomenon. In *Perovskite Photovoltaics*, pages 163–196. Elsevier, 2018.

[12] Henry J Snaith, Antonio Abate, James M Ball, Giles E Eperon, Tomas Leijtens, Nakita K Noel, Samuel D Stranks, Jacob Tse-Wei Wang, Konrad Wojciechowski, and Wei Zhang. Anomalous hysteresis in perovskite solar cells. *The journal of physical chemistry letters*, 5(9):1511–1515, 2014.

[13] Sergiu Draguta, Siddharatha Thakur, Yurii V Morozov, Yuanxing Wang, Joseph S Manser, Prashant V Kamat, and Masaru Kuno. Spatially non-uniform trap state densities in solution-processed hybrid perovskite thin films. *The journal of physical chemistry letters*, 7(4):715–721, 2016.

[14] Weike Zhu, Shurong Wang, Xin Zhang, Aili Wang, Cheng Wu, and Feng Hao. Ion migration in organic–inorganic hybrid perovskite solar cells: Current understanding and perspectives. *Small*, page 2105783, 2022.

[15] Yongbo Yuan and Jinsong Huang. Ion migration in organometal trihalide perovskite and its impact on photovoltaic efficiency and stability. *Accounts of chemical research*, 49(2):286–293, 2016.

[16] Lucie McGovern, Moritz H Futscher, Loreta A Muscarella, and Bruno Ehrler. Understanding the stability of mapbbr3 versus mapbi3: suppression of methylammonium migration and reduction of halide migration. *The journal of physical chemistry letters*, 11(17):7127–7132, 2020.

[17] Congcong Wang, Benjamin R Ecker, Haotong Wei, Jinsong Huang, and Yongli Gao. Environmental surface stability of the mapbbr3 single crystal. *The Journal of Physical Chemistry C*, 122(6):3513–3522, 2018.

[18] Sayantan Mazumdar, Ying Zhao, and Xiaodan Zhang. Stability of perovskite solar cells: Degradation mechanisms and remedies. *Frontiers in Electronics*, page 8, 2021.

[19] Best research-cell efficiency chart. https://www.nrel.gov/pv/cell-efficiency.html. Accessed: 2022-02-04.

[20] Akihiro Kojima, Kenjiro Teshima, Yasuo Shirai, and Tsutomu Miyasaka. Organometal halide perovskites as visible-light sensitizers for photovoltaic cells. *Journal of the american chemical society*, 131(17):6050–6051, 2009.

[21] Michael M Lee, Joël Teuscher, Tsutomu Miyasaka, Takurou N Murakami, and Henry J Snaith. Efficient hybrid solar cells based on meso-superstructured organometal halide perovskites. *Science*, 338(6107):643–647, 2012.

[22] Hui-Seon Kim, Chang-Ryul Lee, Jeong-Hyeok Im, Ki-Beom Lee, Thomas Moehl, Arianna Marchioro, Soo-Jin Moon, Robin Humphry-Baker, Jun-Ho Yum, Jacques E Moser, et al. Lead iodide perovskite sensitized all-solid-state submicron thin film mesoscopic solar cell with efficiency exceeding 9%. *Scientific reports*, 2(1):1–7, 2012.

[23] Michael Saliba, Juan-Pablo Correa-Baena, Christian M Wolff, Martin Stolterfoht, Nga Phung, Steve Albrecht, Dieter Neher, and Antonio Abate. How to make over 20% efficient perovskite solar cells in regular (n–i–p) and inverted (p–i–n) architectures. *Chemistry of Materials*, 30(13):4193–4201, 2018.

[24] Laura Basiricò, Andrea Ciavatti, and Beatrice Fraboni. Solution-grown organic and perovskite x-ray detectors: A new paradigm for the direct detection of ionizing radiation. *Advanced Materials Technologies*, 6(1):2000475, 2021.

[25] Chengxi Zhang, Dai-Bin Kuang, and Wu-Qiang Wu. A review of diverse halide perovskite morphologies for efficient optoelectronic applications. *Small Methods*, 4(2):1900662, 2020.

[26] P Blood. *The electrical characterization of semiconductors : majority carriers and electron states.* Academic Press, London, 1992.

[27] JA Van Vechten and CD Thurmond. Entropy of ionization and temperature variation of ionization levels of defects in semiconductors. *Physical Review B*, 14(8):3539, 1976.

[28] Carlo Lamberti. *Characterization of semiconductor heterostructures and nanostructures.* Elsevier, Amsterdam Oxford, 2008.

[29] Xavier Mathew. Photo-induced current transient spectroscopic study of the traps in cdte. *Solar energy materials and solar cells*, 76(3):225–242, 2003.

[30] Makhsud I Saidaminov, Ahmed L Abdelhady, Banavoth Murali, Erkki Alarousu, Victor M Burlakov, Wei Peng, Ibrahim Dursun, Lingfei Wang, Yao He, Giacomo

Maculan, et al. High-quality bulk hybrid perovskite single crystals within minutes by inverse temperature crystallization. *Nature communications*, 6(1):1–6, 2015.

[31] Smaïl Amari, Jean-Marie Verilhac, Eric Gros DâAillon, Alain Ibanez, and Julien Zaccaro. Optimization of the growth conditions for high quality ch3nh3pbbr3 hybrid perovskite single crystals. *Crystal Growth & Design*, 20(3):1665–1672, 2020.

[32] JC Balland, JP Zielinger, C Noguet, and M Tapiero. Investigation of deep levels in high-resistivity bulk materials by photo-induced current transient spectroscopy. i. review and analysis of some basic problems. *Journal of Physics D: Applied Physics*, 19(1):57, 1986.

[33] Vincenzo Pecunia, Jing Zhao, Chaewon Kim, Blair R Tuttle, Jianjun Mei, Fengzhu Li, Yueheng Peng, Tahmida N Huq, Robert LZ Hoye, Nicola D Kelly, et al. Assessing the impact of defects on lead-free perovskite-inspired photovoltaics via photoinduced current transient spectroscopy. *Advanced Energy Materials*, 11(22):2003968, 2021.